

WORLD METEOROLOGICAL ORGANIZATION

**THIRD MEETING OF WMO TASK TEAM ON
METEOROLOGICAL
ANALYSES FOR FUKUSHIMA-DAIICHI NUCLEAR
POWER PLANT ACCIDENT**

VIENNA, AUSTRIA, 3 – 5 DECEMBER 2012



ANNEX III

The World Meteorological Organization's Evaluation of Meteorological Analyses for the Radionuclide Dispersion and Deposition from the Fukushima Daiichi Nuclear Power Plant Accident

Roland Draxler, Dèlia Arnold, Stefano Galmarini, Matthew Hort, Andrew Jones, Susan Leadbetter, Alain Malo, Christian Maurer, Glenn Rolph, Kazuo Saito, René Servranckx, Toshiki Shimbori, Efisio Solazzo and Gerhard Wotawa

24 January 2013

1. Introduction

The World Meteorological Organization (WMO) organized a small Task Team (TT) to respond to a request from the United Nations Scientific Committee on the Effects of Atomic Radiation (UNSCEAR) to assist them with the meteorological aspects of a dose assessment from the radiological releases from the Fukushima Daiichi nuclear power plant accident. The TT's primary mission was to examine how the use of meteorological analyses and the introduction of additional meteorological observational data, could improve atmospheric transport, dispersion and deposition calculations, a critical component to the dose computations. Although the TT would not be doing dose computations directly for the UNSCEAR assessment, the members agreed that the best way to evaluate the suitability of the various meteorological analyses for the assessment was to actually use the meteorological data in Atmospheric Transport Dispersion and Deposition Models (ATDM) and compare the model predictions against radiological monitoring data.

The TT consisted of participants from the Canadian Meteorological Centre (CMC), the U.S. National Oceanic and Atmospheric Administration (NOAA), the Met Office UK (UKMET), the Japan Meteorological Agency (JMA), and the Austrian Zentralanstalt für Meteorologie und Geodynamik (ZAMG). Representatives from the European Joint Research Centre (Ispra, Italy) were later invited to participate in the data analysis phase of the effort.

The methodology for evaluating the meteorological analyses by computing the dispersion and deposition and comparing these calculations with measurement data was designed during the first meeting (WMO, 2011) of the TT in Geneva and then updated during the TT's second meeting in London (WMO, 2012). The general approach was that each of the TT participants would run their own Atmospheric Transport and Dispersion Model (ATDM) using the meteorological data analysis fields already available to them and the higher spatial and temporal resolution fields provided by JMA. The ATDM calculations would be standardized as much as possible in terms of input and output parameters but each ATDM would retain its unique treatment of the meteorological input data, dispersion, and deposition computations, thereby providing a range of solutions due to variations in model parameterizations as well as the driving meteorological analysis data.

Although the direct evaluation of meteorological analyses without the additional uncertainty introduced by the ATDM calculations is possible by comparing weather observations with the analyses, the time and space integrated nature of the ATDM calculation presents a more realistic evaluation metric. Therefore, the TT decided that the ATDM-meteorology computational results should be compared to the total accumulated deposition for Cs-137. Naturally the evaluation of the ATDM calculations relies not only upon the

meteorological data, but also upon the time varying source term used in the calculation, which was provided to the TT by the UNSCEAR source reconstruction group.

The five TT members provided a total of 20 ATDM-meteorology simulations. As a final product of the TT, the meteorological analyses, the individual ATDM air concentration and deposition calculations, and the ensemble mean calculations were made available to the UNSCEAR community. As part of the evaluation process, the unit-source dispersion and deposition calculations were posted on a web page (http://ready.arl.noaa.gov/READY_fdnpwmo.php) hosted by one of the TT members, which provided a way for the UNSCEAR emission group to test various emission scenarios and compare the results to measured deposition and air concentration data. Prior to receiving the UNSCEAR source term, the TT analyses were done using source term data available at that time, in particular the information published by JAEA (e.g., Chino et al., 2011). Once the source term was finalized by UNSCEAR, these values were then used to compute air concentration and deposition for 14 radionuclides. The air concentration and deposition calculations provided to UNSCEAR used the results from the ensemble mean of the 10 ATDM-meteorology combinations that best represented the range of uncertainty expected in the computations. These results were also posted to an FTP server (<ftp://arlftp.arlhq.noaa.gov/117/UNSCEAR/netcdf>). In addition, the UNSCEAR dose group could run their own dose models using the meteorological data or use the air concentrations and deposition calculations provided by the TT.

2. Meteorological overview of the accident

A summary of the meteorological conditions during the critical phases of the atmospheric emissions was described in the first TT report (WMO, 2011) and several other researchers (Morino et al., 2011; Kinoshita et al., 2011; Korsakissok et al., 2011; Stohl et al., 2012; Sugiyama et al., 2012). The key results follow:

March 9th – 11th: A weak low pressure trough over eastern Japan from March 9th to 11th caused light rain to be observed from the 9th to the morning of the 12th.

March 12th – 13th: A high pressure system moved eastward along the south coast of the main island of Japan from the 12th through the 13th. The wind direction was from the south below 1 km and from the west above 1 km in the afternoon of March 12, the time of the hydrogen explosion at reactor number one.

March 14th - 17th: Another weak low pressure trough moved eastward off the southern coast of the main island from the 14th to the 15th and then moved toward the northeast while developing rapidly after the 15th. Light rain was observed from the 15th to the morning of the 17th due to a weak low pressure system which moved north eastward off the east coast of Japan. In particular, rain was observed in the Fukushima prefecture during the night from 1700 JST March 15 to 0400 JST March 16 (Kinoshita et al., 2011), a time corresponding with significant emissions. The low level winds were from the southwest during the morning of the 14th, the time of the hydrogen explosion at reactor number three. The 950 hPa winds were from the west until the morning of 15th, but changed to a direction from north northeast during the daytime of the 15th, the time when the reactor number two container burst. Chino et al. (2011) estimated the maximum I-131 emissions occurred between 0900-1500 JST (0000-0600 UTC). After 1500 JST, the winds turned to a direction from east southeast, and then changed to north after 0000 JST on the 16th (1500 UTC 15th).

March 18th – 19th: High pressure dominated during this period and winds were generally from the west.

March 20th – 22nd: A low pressure system passed over the main island from March 20th to the 22nd causing moderate rain in the Kanto area (Ibaraki, Chiba, Tochigi, Saitama and in Tokyo) from the 20th to the 23rd.

In addition, several modelling studies have already been conducted, from the local scale examining the major contamination episode of March 15th (Chino et al., 2011) to a more regional scale covering Japan (Morino et al., 2011) to the global scale (Takemura et al., 2011). The modelling results generally support the case that the high deposition area over the middle of the Fukushima prefecture was primarily caused by the deposition that occurred on March 15th.

A detailed evaluation by Korsakissok et al. (2011) found that the meteorological models used in their calculations did not reproduce the wind direction observed on March 15 near the Daiichi NPP between 1800 and 2400 JST. Their models indicated a swing of the wind direction (return of the plume towards the south) whereas the local observations continued to suggest transport towards the northwest (wind directions from east to south), turning towards the south a few hours later. They highlighted that the timing of the releases, with wind direction changes, and precipitation was crucial to reproduce the dose rates and the deposition observed to the northwest of the NPP.

The first WMO TT report (WMO, 2011) briefly summarized some of the available meteorological data and proposed that the Japan Meteorological Agency (JMA) mesoscale analysis would be the most suitable for local and regional scale atmospheric transport, dispersion and deposition modelling over Japan. A cursory examination of the JMA mesoscale wind directions shown in the WMO report for 2100 JST on the 15th indicated winds were from the southeast, which is comparable to the observed direction near the NPP as reported by Korsakissok et al. (2011).

A modelling study by Morino et al. (2011) used the JMA's mesoscale analysis to provide initial and boundary conditions, and also input for grid nudging for the Advanced Weather and Research Forecast (WRF) model (Skamarock et al., 2008), which was used to create meteorological fields at even higher spatial and temporal resolutions. These fields were then used by the Community Multiscale Air Quality (CMAQ) model (Byun and Schere, 2006) to simulate the radionuclide transport and deposition. These results are consistent with those of other studies (Srinivas et al., 2012) which found that the deposition around Fukushima occurred primarily during two periods, 15-17 and 20-26 of March.

Due to the east coast position of the Fukushima Daiichi NPP the TT evaluation, relying on air concentration and deposition data gathered over Japan, is very sensitive to the coincidence of release events and periods of winds from the east and, for the deposition predictions, on days when precipitation occurred. Figure 1 illustrates this phenomena sensitivity. This figure presents the time evolution for both the JAEA (green line) and UNSCEAR (red line) source terms. Beyond the 17th both source rates are identical and therefore only one line can be seen in the figure for Cs-137. The figure also shows, for a constant 1 Bq/hr release rate, (blue line with square symbols) the percentage of the total modelled deposition (calculated using UKMET-ECMWF) for Cs-137 within the area of observed contamination, occurring due to each three-hour source period over March. The integral of this line adds up to 100% i.e. the entire modelled deposition in the specified region. This normalised deposition value shows four distinct periods; 14-16, 20-23, 24-26 and 29-31 in March where the deposition results are particularly sensitive to any changes of the source term. Conversely source term changes outside of these periods have negligible impact on the deposition data though they may of course have significance for air concentration values.

We can illustrate this further by considering the period from midnight of the 14th to the 16th. In this case the Cs-137 emissions for the single three-hour period starting at 0600 JST 15 March (21 UTC 14 March) represents 20% of the total Cs-137 emissions for the entire computational period (11-31 March). Combined with the meteorology, this one three-hour emission period accounts for 30% of the total deposition, based on the UKMET-ECMWF predictions using the UNSCEAR source. This enhanced the simulated deposition pattern to the southwest, a result however not fully consistent with the deposition measurements reported by other researchers (e.g., Korsakissok et al., 2011). For the UNSCEAR source term, releases in the period 14-16

March based on the UKMET-ECMWF predictions are responsible for 67 % of the total deposition within the area of the actual observations used in this study. Katata et al. (2012) reported that most of the observed high density deposition patterns in the Fukushima prefecture were caused by releases in this period.

3. Meteorological analyses available for the evaluation

The meteorological analyses available to the TT were obtained from various sources, each with different horizontal, vertical, and temporal resolution. The meteorological data analyses used in the ATDM computations are described briefly in this section.

3.1 CMC-GEM

The Canadian Meteorological Centre (CMC) is part of the Meteorological Service of Canada (MSC) and is the national centre for numerical weather prediction. CMC runs operationally a complete integrated suite of numerical weather prediction (NWP) models under the Canadian modelling infrastructure called the Global Environmental Multiscale (GEM) system (Côté et al., 1998a; Côté et al., 1998b). This NWP system is executed in a global configuration called Global Deterministic Prediction System (GDPS, CMC 2009; Bélair et al., 2009; Charron et al., 2012) as well as in a regional configuration over North America, i.e. the Regional Deterministic Prediction System (RDPS, Mailhot et al., 2006; Fillion et al., 2010; Tanguay et al., 2012; CMC 2012). Both global and regional configuration systems include a 4D-Var data assimilation system (Gauthier et al., 2007; Laroche et al., 2007). The RDPS represents the main deterministic model used in Canada.

The GDPS is run twice a day (00 and 12 UTC) while the RDPS is run four times a day (00, 06, 12, 18 UTC). Forecasts from the GDPS are valid up to 240 hours (10 days) for the 00 UTC cycle run and up to 180 hours (7.5 days) for the 12 UTC run. Hourly forecasts are available up to 144 hours (6 days) and subsequently at 3-h intervals. Analyses from the GDPS are available at a 6-hour frequency at 00, 06, 12, 18 UTC. The horizontal grid mesh of the GDPS is defined at 33 km (0.3° horizontal resolution) along a meridian or line of longitude and the vertical discretization is done over 80 hybrid-pressure levels. A post-processing task of the GDPS interpolates the data from the native hybrid-pressure coordinate system (lid at 0.1 hPa, i.e. ~64 km AGL) to the standard eta coordinate system on 58 vertical levels (lid at 10 hPa, i.e. ~31 km AGL). This global meteorological analyses database is used to drive CMC's ATDM. A total of 30 eta vertical levels were selected for the ATDM calculations including 14 levels within the 2-km AGL above ground layer (AGL; below ~800 hPa) in order to resolve properly physical processes taking place in the atmospheric boundary layer (ABL).

3.2 NOAA-GDAS

NOAA's National Weather Service's National Centers for Environmental Prediction (NCEP) runs a series of computer analyses and forecasts operationally. One of the systems is the GDAS (Global Data Assimilation System) using the same model as the Global Forecast System (Kanamitsu, 1989; Kanamitsu et al., 1991). The GDAS is run 4 times a day (00, 06, 12, and 18 UTC). Model output is for the analysis time and 3, 6, and 9-hour forecasts. Post-processing of the GDAS converts the data from spectral coefficient form to half degree latitude-longitude grids and from sigma levels to mandatory pressure levels. The successive analyses and three-hour forecasts four times each day produce a continuous data archive. The NOAA transport, dispersion, and deposition calculation used the GDAS data on the native hybrid vertical coordinate system and calculations by ZAMG (FLEXPART) used the GDAS data on isobaric levels.

3.3 ECMWF

The European Centre for Medium-Range Weather Forecasts (ECMWF) produces a high-resolution global forecast twice daily at 00 UTC and 12 UTC. The base model for the operational deterministic forecast is the

Integrated Forecast System (IFS), see Simmons et al. (1989), a comprehensive earth-system model developed at ECMWF. It is a spectral NWP model using a 4D-Var data assimilation system, see Rabier et al. (2000) and Mahfouf and Rabier (2000). Archived model fields have been extracted from the ECMWF MARS archive at a temporal resolution of three hours as a sequence of short-period forecasts at T+3, T+6, T+9 and T+12 from successive forecast cycles of the operational global model.

A selection of meteorological fields was retrieved by the UK Met Office for use in NAME and HYSPLIT and by ZAMG for use in FLEXPART. Fields are encoded as GRIB-1 and GRIB-2 depending on the parameter involved and can be decoded using the ECMWF GRIB_API. It was agreed by the TT that use of the ECMWF global data would provide a further option for running a scenario using the same input meteorology in each dispersion model, and therefore these files were provided to other TT members for the purposes of this study. Meteorological fields were retrieved on a regular latitude-longitude grid at 0.125 degree by 0.125 degree resolution by UKMET and 0.2 degree by 0.2 degree resolution (additionally 0.1 degree and 0.1 degree) by ZAMG over a region centred on Japan. The ECMWF global model has 91 vertical levels.

3.4 UKMET

The operational global configuration of the Met Office Unified Model, MetUM, (Davies et al., 2005) was used for this study. The global version of the Unified Model uses an incremental 4D variational data assimilation system (4D-Var). Forecasts are produced on a six-hour cycle to give four forecast runs per day. Model fields are output for NAME at a temporal resolution of three hours, and archive data therefore consist of alternating model analyses and three-hour forecasts. Meteorological fields from the global model have an approximate horizontal resolution of 25 km in mid latitudes, with 70 vertical levels extending to an altitude of 80 km (but only the lowest 59 model levels up to approximately 30 km are used for NAME applications). Meteorological data is interpolated in both space and time within NAME.

3.5 JMA-MESO

To assist in the regional ATDM calculations, JMA provided their mesoscale analyses fields to the TT and UNSCEAR for the period 11 – 31 March 2011, at three-hourly intervals and at a 5-km horizontal resolution. The mesoscale analyses (MESO) are produced by an operational non-hydrostatic 4D-VAR system of JMA and assimilate a variety of local meteorological observations, including GPS-derived total precipitable water vapour and JMA radar/rain gauge analysed precipitation (RAP; section 3.6; see Honda et al., 2005, Saito et al., 2007 and Honda and Sawada, 2008 for more detailed discussions). All analysis fields are produced by a three hour forecast of the outer-loop model of 4D-VAR with a horizontal resolution of 5 km. The MESO output covered 719 (x-direction) by 575 (y-direction) grid points on a Lambert Conformal projection (30N and 60N at 140E), up to about 21 km above ground. There are in total 50 levels, including 11 levels below 1 km AGL.

Figure 2a shows surface precipitation by JMA-MESO for 1200-1500 UTC, 15 March 2011, one of the critical deposition episodes. Comparison with rainfall distribution (upper) suggests that most of surface precipitation over northern Japan during this period was brought by snow except some of the coastal areas.

3.6 JMA-RAP (Radar-rain gauge Analyzed Precipitation)

JMA also provided a radar-rain gauge-analyzed precipitation dataset (Nagata, 2011) at 30 minute intervals, with a horizontal resolution of 45 seconds in longitude and 30 seconds in latitude covering a region from 118-150 degrees east longitude and from 20-48 degrees north latitude (2560 by 3360 grid points). Several of the ATDM calculations used global meteorological analysis in combination with the high resolution radar rain gauge precipitation.

A comparison of the MESO precipitation, which is a three-hour accumulated model prediction, with the analysis precipitation (RAP) at 30 minute intervals is shown in Figure 2. This illustrates a good agreement of JMA-MESO and RAP precipitation. A circle-shaped small intense precipitation area is seen around the weather Doppler radar site at Sendai (381.3N, 140.91E) for 1130-1330 UTC (upper, Figure 2b), which is due to a bright-band observed by the Sendai radar.

The meteorological analyses used in the ATDM computations are summarized in Table 1. The column headings refer to the producing centre while the acronym row indicates how the meteorological analysis is referred to in the text. Note that the ATDM calculations using a particular meteorology denoted by –R or –RAP used the JMA-RAP precipitation analysis rather than the precipitation field native to that particular meteorological analysis.

Both, the JMA precipitation data and the meteorological analyses described in the previous section (JMA-MESO) were made available to the UNSCEAR community through a WMO hosted password protected web site with read instructions and a file converter kit for different coordinate systems. The data are available to the scientific community for research purposes with acknowledgement. Researchers should contact WMO (dpfsmail@wmo.int).

4 Salient features of each ATDM

Each of the five TT members used a different ATDM, each using one or more of the meteorological analysis data summarized in Table 1. Except for the MESO analysis from the JMA, all the other meteorological model data are from global analyses routinely available at the meteorological centres and to most researchers.

All the TT ATDMs used for this analysis are of a class of models commonly called Lagrangian Particle Dispersion Models (LPDM). A large number of model pollutant particles (by convention called “particles” but that are computational “point” entities that may be treated as a particle or gases), are released from the source location each time step and passively follow the wind, composed of a mean and turbulent components. The mean component is obtained directly from the meteorological data wind field while the turbulent component of the motion, which defines the dispersion of the pollutant cloud, is typically estimated from the meteorological fields based upon various stability and turbulence functions. Although these functions may share common features, their implementation will be unique to each ATDM. Refer to the main citations for each ATDM for a general description of each model. The following sub-sections describe some of the key elements in each ATDM that are different from the other ATDMs and might contribute to some of the differences in the computational results.

4.1 CMC-MLDP0

MLDP0 (*Modèle Lagrangien de Dispersion de Particules d'ordre 0*) is a Lagrangian particle dispersion model of zeroth order designed for long-range dispersion problems occurring at regional and global scales and is described in details in D'Amours and Malo (2004) and D'Amours et al. (2010). Dispersion is estimated by calculating the trajectories of a very large number of air particles (also called parcels or fluid elements). Large scale transport is handled by calculating the displacement due to the synoptic component of the wind field and diffusion through discretized stochastic differential equations to account for the unresolved turbulent motions. Vertical mixing caused by turbulence is handled through a random displacement equation (RDE) based on a diffusion coefficient K_z . The calculation of the diffusion coefficient combines two formulations following Delage (1997), for the surface layer, and O'Brien (1970), for the above layers, in order to produce a vertical profile of K_z consistent with the depth of the ABL (due to the reflection condition at the top of the ABL). This coefficient is calculated in terms of a mixing length, stability function, and vertical wind shear. Lateral mixing (horizontal

diffusion) is modelled according to a first order Langevin Stochastic Equation for the unresolved components of the horizontal wind (mesoscale fluctuations).

MLDP0 is an off-line model that uses the full 3-D meteorological fields provided by a NWP system. Therefore fields of wind, moisture, temperature and geopotential heights must be provided to the model, which are normally obtained from the GEM model forecasts and objective analysis systems in either global, regional or high resolution configuration.

In MLDP0 a particle (or parcel) is assumed to represent the ensemble average of a large number of “real” particles (aerosols or gases). At the emission, it is assigned a mass which depends on the total quantity of material emitted and the total number of particles. The effect of radioactive decay, wet scavenging, dry deposition and gravitational settling can be simulated by calculating the amount of material removed from the carrier particle, when it travels in regions of the atmosphere where such processes are active.

Dry deposition occurs when a particle is subjected to a reflection at the ground surface. It is modelled in terms of a dry deposition velocity v_d and an absorption probability P . The absorption probability is calculated according to Wilson et al. (1989) as

$$P = 1 - R, \quad R = \frac{1 - a}{1 + a}, \quad a = \left(\frac{\pi}{2} \right)^{1/2} \frac{v_d}{\sigma_w},$$

where R is the reflection probability and σ_w is the variance of the vertical turbulent wind component. Since a particle represents the mean of an ensemble of particles, the fraction of the mass removed by dry deposition is equal to P . The deposition rate is calculated by assuming that a particle contributes to the total surface deposition flux in proportion to the tracer material it carries when it is found in a layer adjacent to the ground surface. Dry deposition increment dm_d for particle p over a model time step dt can be expressed as

$$dm_d = P \cdot m_p = (1 - R) \cdot m_p,$$

where m_p is the particle mass. The new particle mass m'_p is then adjusted accordingly

$$m'_p = R \cdot m_p.$$

Wet deposition is treated with a simple scheme and will occur when a particle is presumed to be in a cloud (*in-cloud scavenging*) and is modelled in terms of a wet scavenging rate. Below-cloud scavenging is not considered yet in the operational version of MLDP0. The tracer removal rate is proportional to the local cloud fraction f_c and the particle mass m_p . Wet deposition increment dm_w for particle p over a model time step dt and updated particle mass are calculated using the following relationships

$$dm_w = m_p \cdot [1 - \exp(-s_w f_c dt)],$$

$$m'_p = m_p \cdot \exp(-s_w f_c dt),$$

where s_w is the wet scavenging rate (s^{-1}). Local cloud fraction is parameterized according to Pudykiewicz (1989) as a function of relative humidity following

$$f_c = \frac{U - U_t}{U_s - U_t}, \quad \text{if } U \geq U_t,$$

where f_c is the cloud fraction, U is the relative humidity, U_t is the threshold value of the relative humidity above which the subgrid scale condensation occurs (75% is the default value in MLDP0), U_s is the relative humidity for the saturation state (100%). Local cloud fraction can be estimated in both hindcast and forecast modes, using analysed and forecast NWP meteorological fields.

Gravitational settling in the trajectory calculations is computed according to Stokes' law for fine particles. By default, MLDP0 is run neglecting gravitational settling effects. However, this optional removal process can be included accounting together for a particle size distribution and density of a particle. This process represents an important removal mechanism in atmospheric transport modelling and can modify significantly modelled airborne concentrations and total ground deposition as short scale (near the source) as well as at very long range. This impact is related especially to the particle size distribution used in the modelling. In order to properly model this physical process, it is therefore necessary to have a good knowledge of particle size distribution, something that is rarely known or available.

In MLDP0, tracer concentrations at a given time and location are obtained by assuming that particles carry a certain amount of tracer material. The concentrations are then obtained by calculating the average residence time of the particles, during a given time period, within a given sampling volume, and weighting it according to the material amount carried by the particle. Concentrations are expected to be estimated more accurately near the source with a Lagrangian model than with an Eulerian model.

It is important to note that in MLDP0, all concentrations are averaged in space and time. The concentrations are averaged in the vertical layers and in the horizontal (surrounding grid points weighting algorithm) for smoothing effects and artificial noise attenuation as well as over the output time period/step/resolution specified by the modeller. For example, concentration outputs at 3-h time steps would correspond to average values over that 3-h period.

Three generic species were modelled as surrogates for the radionuclides: a gas with no wet or dry scavenging to mimic noble gases (such as ^{133}Xe), a gas with a relatively large dry deposition velocity (1 cm/s) and wet removal rate ($3 \times 10^{-4} \text{ s}^{-1}$) to represent a depositing gas (such as gaseous ^{131}I), and a particle with a small dry deposition velocity (0.1 cm/s) and wet scavenging rate ($3 \times 10^{-5} \text{ s}^{-1}$) to represent light particles (such as ^{137}Cs or particulate ^{131}I). Details are shown in Table 4.

4.2 HYSPLIT

The calculation of the transport and dispersion from the source was done using the Hybrid Single-Particle Lagrangian Integrated Trajectory (HYSPLIT – Draxler and Hess, 1998) model. A detailed description of the computational aspects of the model can be found in Draxler and Hess (1997) and its configuration is reviewed in the User's Guide (Draxler, 1999).

The special extract of the NOAA GDAS meteorological data archive used for the HYSPLIT ATDM calculations was available on the native hybrid sigma levels. Approximately 15 levels were available below 850 hPa and the remainder continued up to about 10 hPa. The three dimensional fields included the horizontal winds, temperature, and humidity. Vertical velocities were computed in HYSPLIT by integrating the divergence. The other fields used in the calculations include the surface heat and momentum fluxes for the computation of vertical mixing, the boundary layer depth, and the precipitation rate. The ECMWF data fields had comparable number of data fields and vertical resolution to the GDAS but included the vertical velocity field.

In HYSPLIT, scavenging is parameterized through removal constants β (s^{-1}), where the deposition D over time step Δt for each particle of mass M is

$$D = M \{1 - \exp[-\Delta t (\beta_{dry} + \beta_{gas} + \beta_{inc} + \beta_{bel})]\}.$$

The particle mass is reduced by D each time step. The time constant for within-cloud removal for particulate pollutants is

$$\beta_{inc} = S P \Delta Z_p^{-1},$$

where S is the ratio of the pollutant's concentration in water to its concentration in air (4×10^4), ΔZ_p is the depth of the pollutant layer, and the precipitation rate P is the value predicted by the meteorological model used in the calculation. Below-cloud removal is defined directly as a rate constant ($\beta_{bel} = 5 \times 10^{-6}$), independent of the precipitation rate. The wet deposition of gases depends upon their solubility and for inert non-reactive gases it is a function of the Henry's Law constant (H - Molar atm^{-1}), the ratio of the pollutant's equilibrium concentration in water to that in air. Therefore, the gaseous wet removal time constant is

$$\beta_{gas} = H R T P \Delta Z_p^{-1},$$

where R is the universal gas constant ($0.082 \text{ atm M}^{-1} \text{ K}^{-1}$), T is temperature, and the wet removal of gases is applied at all levels from the ground to the top of the cloud-layer. The dry deposition calculation is limited to particles within the surface layer (ΔZ_p is usually about 75 m), and the time constant is

$$\beta_{dry} = V_d \Delta Z_p^{-1}.$$

One critical aspect for quantitative predictions of air concentration is the wet and dry scavenging that occurs along the transport pathway. The computational details are given below. Four generic species were tracked as surrogates for the radionuclides: a gas with no wet or dry scavenging, a gas with a relatively large dry deposition velocity (0.01 m/s) and wet removal (Henry's constant = 0.08) to represent gaseous I-131, a particle with a small deposition velocity (0.001 m/s), and a particle with a large deposition velocity (0.01 m/s). There can be considerable variability in scavenging coefficients and the wet scavenging coefficients used in these calculations are lower than the original model default values (Draxler and Hess, 1997; Hicks, 1986) but these lower values are consistent with the results from more recent deposition studies (Cohen et al., 2002) using the HYSPLIT scavenging parameterizations.

4.3 UKMET-NAME

NAME (Numerical Atmospheric-dispersion Modelling Environment) is the UK Met Office's Lagrangian particle dispersion model and it is used to model the atmospheric transport and dispersion of a range of gases and particles (Maryon et al., 1999 and Jones et al. 2007). It was originally developed to model the transport of radioactive material following the Chernobyl accident but now has a wide range of applications including simulating releases of hazardous materials (chemical, biological, radiological and nuclear) (Becker et al., 2007, Ryall and Maryon 1998), modelling the transport of ash clouds from volcanic eruptions (Webster et al., 2012, Heard et al., 2012), modelling the airborne transmission of diseases (Burgin et al., 2012, Sanson et al., 2011), forecasting air quality, analysing air pollution episodes (Witham and Manning 2007) and identifying source locations and source strengths (Manning et al., 2011).

In NAME, large numbers of model particles are released into the model atmosphere where each particle represents a certain mass of the material (gases or aerosols) being modelled. These particles are advected within the model atmosphere by input three-dimensional winds from numerical weather prediction models and

turbulent dispersion is simulated by random walk techniques; particle velocities are correlated in time at short ranges while the more simple Wiener process is applied for longer range problems. Gravitational settling of particles and loss processes, such as wet and dry deposition, radioactive decay, cloud gamma (Bedwell et al., 2011) and chemical transformations, are calculated if appropriate.

NAME is typically run using NWP data from the Met Office or ECMWF but can be configured to use data in GRIB2 format from any model provided a suitable variable set is available. NAME can use both limited area and global deterministic data as well as ensemble data (through an in-built ensemble framework). These NWP data sets can be nested both in space and time.

Dry deposition is modelled in NAME using the concept of the deposition velocity, v_d (Webster and Thomson, 2011). The flux of pollutant to the ground, F , is proportional to the concentration, C , of pollutant and is given by

$$F = v_d C$$

where v_d is the constant of proportionality. The deposition velocity can either be specified by the user or is calculated using a resistance analogy

$$v_d = \frac{1}{R_a + R_b + R_c}$$

where R_a is the aerodynamic resistance, R_b is the laminar layer resistance and R_c is the surface resistance. The aerodynamic resistance represents the efficiency with which material is transported to the ground by turbulence and is independent of the material. The laminar layer resistance is used to specify the resistance to transport by diffusion across the thin quasi-laminar layer adjacent to the surface. Different parameterizations for R_b are used for gases and particles. The surface resistance characterizes the resistance to capture by the surface and is dependent on both the pollutant and the underlying surface. For particles, the surface resistance is taken to be zero. For gases, a fixed surface resistance can be specified by the user or, for a selection of gases, a complex land use dependent surface resistance parameterization can be invoked.

The removal of material from the atmosphere by wet deposition is based on the depletion equation

$$\frac{dC}{dt} = \Lambda C$$

where C is the air concentration and Λ is the scavenging coefficient. The scavenging coefficient is given by

$$\Lambda = Ar^B$$

where r is the rainfall rate (in mm hr^{-1}) and A and B are coefficients which vary for different types of precipitation (i.e., large-scale/convective and rain/snow) and for different wet deposition processes (i.e., rainout, washout and the seeder-feeder process; see Table 2) (Maryon et al., 1999). Within NAME, wet deposition due to convective and large-scale precipitation are computed separately and summed to give total wet deposition. Material located above the cloud top is not subject to wet deposition. Enhanced wet deposition (due to the seeder-feeder process) is applied to material close to the ground in regions of elevated orography.

4.4 JMA-RATM

The JMA Regional Atmospheric Transport Model (RATM) is the mesoscale tracer transport Lagrangian model which is driven by the MESO analysis (section 3.5). The operational products of RATM in JMA are the photochemical oxidant information or the tephra fall forecast (Shimbori et al., 2010) in Japan. However, RATM was not previously applied to predicting the dispersion and deposition of radionuclides. The model description of RATM can be found in Shimbori et al. (2010) and the references of Saito (2012).

For the prediction of radionuclides with RATM in this task, the deposition schemes were upgraded. Regarding the wet deposition for light particles only washout processes are considered. The below-cloud scavenging rate is given by Kitada (1994):

$$\Lambda_w = 2.78 \times 10^{-5} P^{0.75} \text{ [1/s]}$$

where P is the precipitation intensity [mm/h] given by the three-hour average of the accumulated precipitation of MESO or every 30 minutes of RAP (section 3.6). On the other hand, wet deposition for depositing gas is considered only as a rainout process. The in-cloud scavenging rate is given by Hertel et al. (1995):

$$\Lambda_r = P / \{ [(1-LWC) / 6.56 \times 10^{-3} T + LWC] Z_r \}$$

where LWC is the liquid water content, T is the temperature [K], and Z_r is cloud thickness by MESO. Wet deposition is applied to the tracer particles or gas under the height of about 3000 m in the original RATM and about 1500 m in the revised one.

Dry deposition is simply evaluated with the following deposition rate (Iwasaki et al., 1998):

$$\Lambda_d = V_d / Z_d$$

where V_d is the dry-deposition velocity and Z_d is the depth of surface layer. The value of V_d is set to 1×10^{-3} m/s for light particles or 1×10^{-2} m/s for depositing gas (Sportisse, 2007; Draxler and Rolph, 2012), and Z_d is 100 m for both tracer types.

Furthermore, the gravitational settling is considered for light particles in vertical advection step. These tracer particles follow the Stokes' law with the Cunningham correction coefficient. The grain-size distribution assumes the log-normal with mean diameter of 1 μm and standard deviation of 1.0, particle density is 1 g/cm^3 uniformly. Note that if a tracer particle moves under the model surface in vertical advection or diffusion step, it is forcibly reflected to the mirror symmetric point above the surface.

4.5 ZAMG-FLEXPART

ZAMG uses FLEXPART (Stohl et al. 1998, 2005, <http://transport.nilu.no/flexpart>) in many of its atmospheric transport modelling applications, ranging from emergency response systems to research purposes, specifically applied to nuclear releases (e.g., Stohl et al. 2012). FLEXPART is an off-line model. It can use meteorological fields (analyses or forecasts) from the ECMWF numerical weather prediction model (ECMWF, 1995) on a latitude/longitude grid with native ECMWF model levels, in Gridded Binary (GRIB) format versions 1 or 2. In addition, the newer versions are provided with the source code to enable the use of meteorological fields from NCEP's GFS model on pressure levels. FLEXPART can run on a global or a regional domain and may use up to seven nested meteorological input with increasing horizontal resolution. Other versions of FLEXPART capable of being driven by mesoscale meteorological models such as COSMO or WRF (Fast and Easter 2006,

Brioude et al. 2011, Brioude et al. 2012) have been developed as offshoots. They may differ significantly with respect to the grid systems and the parameterization of turbulence and convection.

FLEXPART can be run in a pure random-walk mode or solving a Langevin equation considering turbulent time scales. The latter is slower but more accurate and better for regional and local applications. The meandering, or mesoscale fluctuations, are solved using a parameterization. Turbulent velocity components are derived from surface heat and momentum fluxes in the input data and a boundary layer height diagnosed within FLEXPART. Turbulence is assumed to be Gaussian. FLEXPART can optionally consider moist convection with a particle relocation matrix diagnosed from the resolved-scale input fields (Forster et al. 2007). FLEXPART output can be produced on a regular latitude-longitude grid with the option of one nested output grid. The output is in a highly efficient binary format.

FLEXPART has a detailed representation of dry deposition and gravitational settling (which may be activated or not). The wet deposition scheme used to be based on a scavenging rate depending only on precipitation intensity and using bulk parameters defined by the user. More recently, a version differentiating between in-cloud and below-cloud scavenging has been released. This differentiation is important since in-cloud scavenging is much more efficient and occurs in a larger volume than the below-cloud scavenging. The current wet deposition scheme assumes clouds are present where the relative humidity exceeds 80% (see <http://transport.nilu.no/flexpart> for further details). This new scheme, however, leads sometimes to unrealistic patterns due to the lack of interpolation of the cloud cover and the rain interpolation. A workaround was developed by P. Seibert for the FLEXRISK Project (<http://flexrisk.boku.ac.at/>) and has been used in the ECMWF-based runs of this study. This quick fix includes the interpolation of the cloud thickness between input times, a new interpolation of the precipitation and a hard-coded modification of the wet deposition scheme that uses the old bulk scheme in case of missing information.

In FLEXPART the deposition processes are expressed by a loss of mass following

$$m(t + \Delta t) = m(t) \exp(-\Lambda \Delta t)$$

and where Λ is the scavenging coefficient which will have a different formulation whether it is below-cloud scavenging or in-cloud scavenging and also depending on the simulated species, being different for gases and aerosols. For below-cloud scavenging, the scavenging coefficient, which will depend on the precipitation intensity, I , is calculated following McMahon and Denison (1979) with

$$\Lambda = A I^B$$

and A and B defined by the user. In this case, A was $8.0E-05 \text{ s}^{-1}$ and $1.0E-04 \text{ s}^{-1}$ for iodine (gas) and Cs-137 (aerosol), and B 0.62 and 0.8.

The in-cloud scavenging follows Hertel et al. (1995) and it has no user-defined parameters. In this case the scavenging coefficient is

$$\Lambda = S_i I H_i^{-1}$$

where Λ is the scavenging coefficient in s^{-1} , I the precipitation intensity and S_i the factor that is different for gases and particles. For particles,

$$S_i = 0.9 \text{ cl}^{-1}$$

and where the cloud liquid content, cl , is $2 \cdot 10^{-7} l^{0.36}$. For gases,

$$S_i = 1 \text{ cleff}^{-1}$$

with $cleff$ being the effective cloud water content.

5 Processing of the JMA-MESO analyses for ATDM applications

Although the original intent of the WMO TT was simply to provide guidance to UNSCEAR about the best meteorology to use for ATDM calculations in the dose assessment and make these data available as needed, it was quickly realized that to perform the evaluation of the meteorological data in this context, it was necessary to apply them in actual ATDM calculations. In that respect the TT felt that an emphasis on using the JMA-MESO analysis data would provide a realistic anchor to the ATDM calculations. However, due to the exact content of the JMA MESO files, the differences in ATDM architecture, coordinate structure, and parameterizations customized to the meteorological data native to the ATDM, the challenge of using the JMA-MESO data was considerable.

In addition to the JMA MESO data and the RAP observations described in Sections 3.5 and 3.6, JMA also provided the TT with a file handling and conversion utility (`conv_jma_grib2`). This utility enabled:

- a) The conversion and potentially interpolation of the MESO and RAP horizontal and vertical (MESO only) coordinate systems onto a regular lat-long and pressure level grid.
- b) The conversion of the RAP data (encoded in GRIB2 format using a compression method representing discrete level values of precipitation intensity based on the maximum precipitation value contained in each file) to precipitation intensities.

The following sections describe some of the pre-processing and modifications required for each ATDM to use the JMA-MESO analyses.

5.1 CMC-MLDP0

Original JMA mesoscale analyses provided to participants were encoded in the WMO-GRIB2 binary format on a Lambert conformal (LC) grid projection at 5 km resolution and on JMA's hybrid vertical coordinate system. CMC's ATDM MLDP0 operates on a polar stereographic (PS) grid, using standard sigma, eta or CMC's hybrid-pressure vertical coordinate system, and ingests meteorological field files (and outputs concentration and deposition files) in an in-house binary format. For these reasons, in order to run MLDP0 with the JMA meteorological analyses, the data were processed following a few steps.

- a) Using the `conv_jma_grib2` converter toolkit, the data were interpolated linearly from the LC grid to a regular latitude-longitude (LL) grid (grid size: 601×481, grid resolution: 0.05°×0.05°, bottom left corner: 23°N,120°E, top right corner: 47°N,150°E). The LL grid is completely nested in the LC grid to avoid numerical extrapolation or processing undefined values.
- b) The data were decoded and converted (on the same latitude-longitude grid defined in previous step) from the WMO-GRIB2 format to CMC's binary format using a GRIB2 decoder software developed in-house.
- c) The 3D pressure fields were used to interpolate the data at each vertical level to the MLDP0 vertical eta coordinate system. Potential temperature was converted to ambient temperature. This pre-processing

step was applied to all required input variables for MLDP0: air temperature, horizontal winds, geopotential height and specific humidity. The vertical motion was not used due to incompatibility issues with MLDP0's computational vertical system of reference (see the next paragraph).

- d) The geometric vertical velocity omega [m/s] in JMA's coordinate is relative to mean sea level (MSL), while MLDP0 expects the vertical velocity omega in hybrid/eta/sigma coordinate relative to model reference system [s-1]. Because of that, the divergence equation was integrated to compute vertical velocities in the appropriate reference system for MLDP0 (equation 6.2 of Côté et al., 1998a). This step was performed within the meteorological pre-processing of MLDP0, which also calculates other missing meteorological variables required by the dispersion model such as the boundary layer height, roughness length, relative humidity, cloud fraction, vertical diffusion coefficient, wind shear and Richardson number. All variables were interpolated on a PS grid projection to meet CMC's ATDM configuration requirements. Again, this PS grid is completely nested in the LL grid to avoid numerical extrapolation or processing undefined values.
- e) Finally, the concentration/deposition unit source results from MLDP0 were interpolated over a LL grid (grid size: 601×401, grid resolution: 0.05°×0.05°, bottom left corner: 28°N, 125°E, top right corner: 48°N, 155°E) and converted to the NOAA-ARL's HYSPLIT compatible binary format. Figure 3 represents the bounding box associated to this post-processing step.

The radar/rain gauge precipitation data provided by JMA was not considered because the operational version of MLDP0 uses relative humidity/cloud fraction in the wet scavenging scheme. However, new dry and wet scavenging parameterizations are currently under evaluation at CMC in a development version of MLDP0. This new scavenging scheme will be tested in the near future using JMA's high resolution radar precipitation fields.

5.2 NOAA-HYSPLIT

A minimum amount of pre-processing was applied to the JMA analyses which contained pressure, potential temperature, horizontal winds, moisture, and vertical velocity. The 3D pressure fields was used directly to map the data at each level to the HYSPLIT vertical sigma coordinate, potential temperature was converted to ambient temperature, and the vertical velocities were first remapped to a terrain following coordinate system consistent with the HYSPLIT computational framework. The vertical velocity correction,

$$\sigma (u \partial \eta / \partial x + v \partial \eta / \partial y)$$

was applied at all levels based upon the slope of the terrain surface (η) and decreasing with height (σ).

With respect to the wet deposition, ATDM calculations used the precipitation fields without adjustment: the MESO analysis 3-hour accumulated precipitation and calculations with the RAP used the precipitation at the grid point nearest in space (~ 1 km) and time (~ 30 min) to each particle at each integration time step.

5.3 JMA-RATM

The motion of tracer particles in RATM is calculated in the same coordinate system as the MESO analysis, i.e., the Lambert conformal conic coordinate on the horizontal surface and terrain-following hybrid coordinate in the vertical direction.

As previously mentioned in section 4.4, the original RATM was not designed to predict radionuclides. Therefore it is necessary to consider the treatment of the instantaneous MESO output, especially the vertical

velocities near the model surface to move depositing gas or light particles. In the revised version of RATM, vertical advection is calculated using the spatially-averaged (9-grid cells) value of the vertical velocities of the MESO and is assumed to be terrain-following at the lowest model level (40 m). Some improper treatments of horizontal and vertical interpolations of the kinematic fields in the original version were also corrected in the revised version. These revisions ameliorate the Cs-137 deposition patterns and significantly improve the statistics of JMA RATM (see table 5). From the point of view of wet deposition process, however, due to the restriction of the current RATM for the ice phase treatment, not total precipitation but liquid rain only (upper, Figure 2a) was considered in the calculation.

In the case of using RAP, instead of the three hourly accumulated precipitation by MESO, the precipitation intensity at each grid point (5-km horizontal resolution) is calculated by the spatial average of surrounding 25-grid cells of RAP (1-km resolution) every 30 minutes.

5.4 UKMET-NAME

Work was undertaken by the Met Office to adapt the NAME dispersion model for use with meteorological input fields derived from the JMA mesoscale analysis and rainfall analysis data sets associated with the period of the Fukushima Daiichi nuclear power plant accident. NAME simulations were performed both with and without replacement of the mesoscale analysis rainfall field by the radar/rain gauge analysis.

Although NAME has some flexibility in its abilities to use different sources of input NWP meteorology, it was not possible to use the JMA data files directly, partly because some of the parameters required by NAME were not available in the data set, but also because the available fields used horizontal and vertical grids that are not supported by NAME. NWP meteorological fields for NAME must be provided on a regular rectangular grid, usually defined in a latitude-longitude (or rotated latitude-longitude) horizontal coordinate system, and the vertical discretisation of 3-d fields must use one of a specific set of terrain-following hybrid vertical coordinate systems (either height-based or pressure-based) but which does not include the JMA hybrid coordinate. A pre-processing step for the JMA analysis files was therefore needed to build NWP files more suited to NAME input requirements.

NAME tends to be rather demanding in terms of its NWP requirements, especially for cloud and precipitation parameters, as these are normally routinely available in the operational forecast files produced at the Met Office. Many of these parameters were missing from the JMA data set and therefore NAME-compatible met files had to be prepared from the set of NWP fields that were available. This included the option of substituting the NWP precipitation field with a replacement field obtained from the hourly radar/rain gauge analysis data set (the rainfall intensities were first processed using the JMA utility `conv_jma_grib2` with the 'mean' interpolation option for re-gridding such that the mean value was calculated from individual data values within each grid cell). Additional parameters were constructed from the available fields where this was necessary, e.g. converting potential temperature to temperature, converting accumulated rainfall to mean rates, and estimating cloud cover and heat fluxes. In particular, the estimation of surface fluxes of heat and momentum followed a similar approach to that used by the HYSPLIT model.

The pre-processing of missing fields was performed in two stages. An initial pass was carried out for parameters that do not depend on roughness length. This first pass calculated missing fields on the original Lambert grid of the JMA mesoscale model. For example, the required cloud information was reconstructed from available humidity and thermodynamic fields, whereas boundary layer depth was estimated using the vertical profile of potential temperature at each grid point. Fields were then re-gridded from the Lambert projection onto a regular latitude-longitude grid with grid length of 0.05 degrees (approximately equivalent to the JMA grid length). Roughness length was missing as a parameter in the JMA data files, and therefore a substitute roughness length was extracted from the ECMWF operational global model (interpolated onto the

same latitude-longitude grid). A second pass through the parameters could then process any fields that required roughness length (e.g. the surface fluxes). Finally, the 3-d multi-level fields originally on the JMA hybrid model levels were interpolated onto a set of Unified Model-style height-based eta levels with an approximately equivalent vertical discretisation as the JMA mesoscale model.

Some basic testing was performed to ensure that coordinate transformations from the Lambert projection to the regular latitude-longitude frame of reference were correct, and that the re-gridded fields were correctly positioned. Further testing was then conducted to inter-compare NAME predictions of the atmospheric transport and deposition obtained using the processed JMA data with those obtained using input meteorological fields from the UM Global and ECMWF Global models. NAME results based on the JMA data are broadly consistent with these other meteorological models in terms of the spatial distributions and magnitudes of air concentration and deposition fields, improving confidence in the methodology adopted for ingesting the JMA data into NAME.

5.5 ZAMG-FLEXPART

The highly resolved MESO- precipitation analysis as well as the even more highly resolved radar-gauge-precipitation analysis were transformed to regular grids of 0.1° , 0.2° , and 0.5° , horizontal resolution via an linear interpolation tool provided by the JMA. The MESO- analysis provides 3-hourly accumulated fields, whereas the radar-gauge analysis contains one-hourly accumulated fields every half an hour, so that in the latter case a proper summing of individual dates was necessary. Further, these gridded, regional data were used to partly replace precipitation fields in the corresponding GRIB messages in the regional ECMWF (0.1° , and 0.2° resolution) and the global NCEP (0.5° resolution) data files. This procedure had to be done in a slightly different way for the two data sets: In the case of the ECMWF- fields, where large scale and convective precipitation are given separately, large scale and convective precipitation were added first and stored in the GRIB message for large scale precipitation. As consequence the convective precipitation had to be set to zero and the FLEXPART routines had to be adjusted to that change. In a second step the ECMWF - values could be replaced by MESO/radar-gauge data whenever possible (i.e. not missing). In case of NCEP- fields, the substitution procedure was easier, since FLEXPART uses the field "total precipitation rate per second". So the MESO/radar-gauge data accumulated over 3 hours only had to be divided by 3×3600 before inserting them in the NCEP- field in order to yield the desired quantity. However, for consistency reasons, the convective precipitation was also set to zero. The overall result of a precipitation comparison (made for the geographical region of 137° - 144° E and 33° - 40° N) is an underestimation of total precipitation by ECMWF compared to the MESO and radar-gauge analysis. In contrast to the NCEP fields, the underestimation is slightly bigger and not compensated by an overestimation in other regions, so that ECMWF fields seem to be biased towards lower than actual precipitation (the radar-gauge values can be considered as "ground truth"). Even taking ECMWF data with 0.1° resolution does not overcome that problem, because one would expect this high-resolution model to perform better than the low-resolution (0.5°) NCEP model, especially in a topographically complex region like Japan.

With respect to the wet deposition, ATDM calculations used the precipitation fields without adjustment: the MESO analysis 3-hour accumulated precipitation and the RAP used the precipitation at the grid point nearest in space (~ 1 km) and time (~ 30 min) to each particle at each integration time step.

6 Description of the ATDM Computational Approach

Air concentrations (or the dilution factors when using a unit source) are computed either by summing each computational particle's mass as it passes over a concentration grid cell and dividing the result by the cell's volume or assigning a fraction of the particle mass to the nearby cells through the usage of a particle density function (kernel) of varying degrees of sophistication (e.g. FLEXPART uses a uniform kernel three hours after

the particle release). In addition, each ATDM may have a slightly different treatment of this calculation depending upon whether a functional particle distribution is assumed between grid cells when the particle density becomes sparse.

One critical aspect for the quantitative predictions of air concentration and deposition is the wet and dry scavenging that occurs along the particle's transport pathway. Because following a large number of radionuclides could be computationally prohibitive, only three generic species were tracked as surrogates for all of the radionuclides: a gas with no wet or dry scavenging (noble), a gas with a relatively large dry deposition velocity and wet removal to represent gaseous I-131, and a particle with wet removal and a small dry deposition velocity to represent all the remaining radionuclide particles. There can be considerable variability in scavenging coefficients and deposition processes. Each ATDM had its own unique treatment of these processes which were described in section 4.

The ATDMs are all run "off-line" meaning that space and time varying meteorological data fields for the computational period must be available to the ATDM. The period of 11 – 31 March 2011 was determined to be the period of greatest interest. Given the uncertainties in the emissions and the temporal frequency of meteorological analyses, the release periods were divided into three-hour duration segments. The emission rate is assumed to be a constant for each three-hour period. A separate 72 hour duration ATDM calculation was made for each radionuclide release period which was sufficiently long to permit particles to exit the regional sampling domain (see Figure 3). After testing the ATDM calculations with several different particle number release rates and considering the regional nature and resolution of the concentration grid, the emissions were represented by the release of 100,000 particles per hour with a total mass of one unit per hour. Because of the uncertainty in the actual value of the time varying release height, particles were uniformly released from ground-level to 100 m.

The ATDM calculations were started every three hours from 11 March 0000 UTC through 31 March 2100 UTC, resulting in 168 independent calculations. All ATDMs used a similar concentration-deposition grid configuration of 601 (west to east) and 401 (south to north) grid cells defined on a regular latitude-longitude grid at 0.05 degrees resolution (about 5 km) centred at 38N and 140E (Figure 3). The output was configured to provide 3-hour averages for air concentrations and 3-hour deposition totals. Air concentration and deposition at any one point in space and time are computed by adding together the contribution of the each of the release period calculations (within that 72 hour window) contributing to desired sampling period.

Because of the fact that emissions were not finalized at the beginning of the TT study, and the undetermined number of radionuclides that might be required, all ATDM computations were done using a unit source emission rate. The calculation for each emission period provides the dispersion and deposition factors from the release point for that emission period to all downwind grid locations, defining how much of the emissions are transferred to each location for every output time period. The set of calculations for all emission times is defined as the Transfer Coefficient Matrix (TCM). When quantitative results are required, the actual air concentrations and depositions are computed in a simple post-processing step by assigning the TCM computational surrogate to a specific radionuclide, multiplying the TCM by the appropriate time-varying emission rates and radioactive decay constant. The UNSCEAR emissions were decay-corrected to 0600 UTC 11 March. Therefore in the post-processing computation of air concentration and deposition, individual radionuclide decay rates are applied starting from the normalization time. Using this methodology, results for multiple emission scenarios can easily be created without rerunning any of the ATDMs. A detailed description of this approach is given by Draxler and Rolph (2012).

A summary of all the ATDM calculations and the meteorological data they used is shown in Table 3. The "C" indicates a completed model simulation and the "R" indicates a completed simulation using the supplemental

radar-rain gauge data provided by the JMA. Eighteen ATDM-meteorology simulations are available for analyses.

7 Radionuclide measurements for model evaluation

In terms of evaluating the meteorological analyses, common statistics of just the meteorological analyses, typically paired in space and time with observations, would not be an adequate measure of the quality of the radionuclide plumes produced using those data because the radionuclide plume structure varies in space and time. The issue is not just a question of which meteorological analyses is the most suitable to use, but how can the ATDM models be optimized to work with the high resolution JMA data, in terms of computing vertical motion, stability, mixing, and deposition. Therefore, the TT concluded that the best overall metric would be to evaluate the ATDM's performance by comparing the model predicted patterns of Cs-137 deposition to the available deposition measurements. The accumulated Cs-137 deposition field has the advantage of the availability of measurements over a wide region. One disadvantage, discussed previously, is that the bulk of the deposition occurred during only a few time periods. In addition, there is considerable interest in how well the ATDM-meteorology combinations can represent the air concentration data. However, in terms of radionuclide specific measurements, air concentration data were available at only a few locations. The TT decided not to use the more abundant gamma dose measurements due to their dependence upon detailed knowledge of the full source inventory.

7.1 Deposition

To perform a quantitative analysis of the ATDM-meteorology combinations requires a digital version of the now well re-published Cs-137 deposition graphic (Figure 4) first reported by the Japanese Ministry of Education and Science and Technology (MEXT) and subsequently published (Kinoshita et al., 2011). However, some of the measurements in digital form contributing to this graphic have been made available elsewhere and have been merged into an equivalent digital product that the TT used for their ATDM-meteorology evaluations. The TT version includes measurements taken by the U.S. Department of Energy's (USDOE, 2011) fixed-wing aircraft (C-12) from 2 April 2011 to 9 May 2011 and ground based measurements by MEXT (MEXT, 2011). The aircraft data were collected using an array of large thallium activated sodium iodide crystals. It was assumed that the data collected early in the period (2 April) could be used as proxy for the total deposition on 31 March (end of the modelling period). The collected aircraft and ground based data points were averaged onto an identical grid (0.05 degree resolution) to that used in the ATDM calculations where the aircraft based sampling covered 374 grid points and blending in the additional ground based data resulted in 543 grid points for model verification. The blended Cs-137 deposition measurements are shown in Figure 5. Note that the TT product captures the deposition in the Fukushima prefecture, but does not include any of the deposition to the southwest. Although these data are considered to be the best available at this time, there may be uncertainties in the representativeness of these data due to the soil permeability, fracturing, and radionuclide solubility, which could result in vertical and horizontal migration of radionuclides in the soil, therefore altering the spatial distribution and strength of the original deposition.

7.2 Air concentration

After the accident at the Fukushima Daiichi Nuclear Power Plant, radiation was monitored at the Nuclear Fuel Cycle Engineering Laboratories, Japan Atomic Energy Agency (JAEA). Furuta et al. (2011) provides preliminary monitoring results of dose rates, air concentrations, and deposition until 31 May 2011. The TT used the time series of Cs-137 and I-131 (aerosol and gas) air concentrations measured at JAEA (Chino, 2012) at location 36.4356N 140.6025E (~110 km SSW of Fukushima Daiichi NPP; see the figure in Appendix A) for the ATDM-meteorology evaluations for the 11-31 March period.

The CTBTO Takasaki sampling site (located at 36.30N 139.08E, ~210 km SW of Fukushima Daiichi NPP) also monitored air concentrations for Cs-137, I-131 and Xe-133 radionuclides. The TT did not consider these data due to unresolved contamination issues.

8 Statistical evaluation methods

Procedures for evaluating ATDM calculations have a long history (Fox 1984; Hanna 1989, 1993; Chang and Hanna 2004). The problem eludes simple solutions because the variability in atmospheric motions cannot be deterministically represented in any model resulting in the inevitable mismatches between predicted and measured concentrations paired in space and time. The ATDM-meteorology evaluation protocol used here follows the procedures used by Mosca et al. (1998) and Stohl et al. (1998). However, only five statistical parameters were selected from their broad list to represent well defined evaluation categories. Both Mosca et al. (1998) and Stohl et al. (1998) recognized the problem in dealing with the uncertainties of “near background” measurement data and avoiding statistical parameters that may be too sensitive to small variations in the measurement values such as ratios between measured and calculated concentration. For a quick evaluation comparison, it is desirable to have a single parameter, which could be used to determine an overall degree of model performance. Stohl et al. (1998) found that the ratio based statistics are the most sensitive to measurement errors while the correlation coefficient is one of the most robust. Chang and Hanna (2004) are more critical of the correlation coefficient due to its sensitivity to high concentrations. Chang and Hanna (2004) also summarized attempts by several different researchers to define a single model evaluation parameter, such as ranking models by each statistic and then ordering by the total rank. In the following evaluation, a new ranking method (Draxler, 2006) was defined by giving equal weight to the normalized (0 to 1) sum of the correlation coefficient (R), the fractional bias (FB), the figure-of-merit in space (FMS), and the Kolmogorov-Smirnov parameter (KSP), such that the total model rank would range from 0 to 4 (from worst to best),

$$\text{Rank} = R^2 + 1 - |\text{FB}/2| + \text{FMS}/100 + (1 - \text{KSP}/100).$$

The correlation coefficient (R), also referred to as the Pearson’s Correlation Coefficient (PCC), is used to represent the scatter among paired measured (M) and predicted (P) values:

$$R = \frac{\sum (M_i - \bar{M})(P_i - \bar{P})}{\sqrt{\sum (M_i - \bar{M})^2 \sum (P_i - \bar{P})^2}},$$

where the summation is taken over the number of samples and the over-bar represents a mean value. A slight variation is introduced in the computation of R. To reduce the sensitivity to outliers, the average correlation is computed by taking the average variance over N iterations, where N is equal to the number of samples, and 20% of the samples, selected randomly, are eliminated from each iteration before computing R. Although strongly influenced by both the correlation and bias, the percentage of calculations within a certain factor of the measured value is a popular statistic, such as within a factor of two (%FA2) or five (%FA5) defined as the percentage of values that satisfy

$$0.5 \leq \frac{P}{M} \leq 2.0 \quad \text{and} \quad 0.2 \leq \frac{P}{M} \leq 5.0.$$

A normalized measure of bias is the fractional bias (FB). Positive values indicate over-prediction and FB ranges in value from –2 to +2 and it is defined by:

$$FB = 2 \frac{(\bar{P} - \bar{M})}{(\bar{P} + \bar{M})} .$$

As discussed in Mosca et al. (1998), by plotting predicted values against measured values, we get a scatter diagram, which can be divided into two regimes: values above the $y=x$ line indicate over-prediction, while values below the line indicate under-prediction. If N pairs (M_i, P_i) are plotted, then $N_{(P_i > M_i)}$ is the number of over-predictions, i.e., the number of pairs where $P_i > M_i$. The factor of exceedance (FOEX) is expressed as a percent value following:

$$FOEX = \left[\frac{N_{(P_i > M_i)}}{N} - 0.5 \right] \times 100, \quad -50 \leq FOEX \leq +50 .$$

A value of FOEX equal to -50% means that all values are under-predicted (all pairs are below the $y=x$ line); on the other hand, a value of +50% means that all values are over-predicted (all pairs above the $y=x$ line). A value of 0% means that there are half under-predictions and half over-predictions (not meaning necessarily that all N pairs lie on the $y=x$ line).

The normalized mean square error (NMSE) is defined as:

$$NMSE = \frac{1}{\bar{M} \cdot \bar{P}} \cdot \frac{1}{N} \sum (M_i - P_i)^2 .$$

The NMSE provides information on the deviations and not on the overestimation/underestimation. Values of NMSE are always positive (Mosca et al., 1998). This parameter is very sensitive to differences between measured and predicted values. Perfect model results would have a NMSE value of zero. A similar metric is the root mean square error (*RMSE*), which is the square root of *NMSE* without normalization by $(M-P)$.

The spatial distribution of the calculation relative to the measurements can be determined from the Figure of Merit in Space (FMS), which is defined as the percentage of overlap between measured and predicted areas. Rather than trying to contour sparse measurement data, the FMS is calculated as the intersection over the union of predicted (p) and measured (m) concentrations in terms of the number (N) of samplers with concentrations greater than a pre-defined threshold (zero):

$$FMS = 100 \frac{N_P \cap N_M}{N_P \cup N_M} .$$

Differences between the distribution of unpaired measured and predicted values is represented by the Kolmogorov-Smirnov parameter, which is defined as the maximum difference between two cumulative distributions when $M_k = P_k$, where

$$KSP = \text{Max} | D(M_k) - D(P_k) | ,$$

and D is the cumulative distribution of the measured and predicted concentrations over the range of k values such that D is the probability that the concentration will not exceed M_k or P_k . It is a measure of how well the model reproduces the measured concentration distribution regardless of when or where it occurred. The maximum difference between any two distributions cannot be more than 100%.

9 Summary of the ATDM Results

9.1 Deposition

The preliminary ATDM results are summarized in Table 5 using the source term originally determined by Chino et al. (2011), modified by Terada et al. (2012), and further revised by Fischer (2012) and is hereafter called the “UNSCEAR” source term. Naturally the model deposition predictions outside of the sampling domain are not considered. But it is clear that there is quite a range of model performance (Ranks from 2.63 to 3.52). A high or low rank with regard to the overall deposition pattern does not suggest that the particular model will perform the same way for air concentrations nor does it mean that the model performance will rank the same way for any one specific emission period. The fact that multiple model results are available permits the computation of a single mean model result to represent the ATDM calculations providing more consistency in the model results at different times and for both deposition and air concentration.

Although some of the ATDM calculations used the same meteorological data source, they may have had the fields available at a different resolution than the other ATDMs using the same meteorological data source, or they may have processed the meteorological data differently. See the individual ATDM documentation in section 3 for more details on this matter. For example, both the UKMET and CMC ATDM calculations using the MESO data showed improved statistical scores over calculations using their global analyses (UKMO, ECMWF and GEM). In contrast the NOAA ATDM calculation scores with the MESO data were clearly inferior to the calculations using global analyses (ECMWF and GDAS).

The sensitivity of the quantitative statistical results to both the model and the meteorology can be appreciated by a more qualitative comparison with the measured deposition patterns holding the model or meteorology constant. Figure 6A shows NOAA model predicted deposition pattern using the ECMWF meteorology (the result with the highest Rank) and Figure 6B shows the NOAA model result using the MESO meteorology (with some of the lower ranking results). Ignoring the offshore component, both simulations show a deposition component to the north that does not exist in the measurements (Figure 4). The pattern to the northwest and west shows a much better fit to the measurements using ECMWF data, while the extension to the south along the coast is unrealistically represented by both calculations, which also depends on the source term used.

The same calculation combination of ECMWF and MESO data, but for the UKMET ATDM is shown in Figure 7. The difference in the ATDM calculations (here NOAA and UKMET) is apparent for calculations using either ECMWF or MESO data. The UKMET results tend to be much smoother than the NOAA calculation which is especially striking for the calculations using the finer resolution MESO data. Although the NOAA calculation shows a distinct left turn in the high deposition region from the northwest to the southwest, also evident in the measurements, the granularity of the deposition pattern in the calculation using the MESO data detracts from the NOAA model’s quantitative performance statistics. The smoother UKMET deposition results, although not necessarily identically aligned with the measurements, are more consistent with the smoother patterns observed in the measured deposition.

The point of this discussion is that there are multiple factors (emissions, meteorology, ATDM assumptions) that may be impossible to isolate which confound a simple evaluation of the best meteorology to use in modelling the deposition and air concentrations. There is additional uncertainty in the metric used to evaluate the model results. For example, in Appendix A, we summarize the model results compared with both, deposition and air concentrations. The ranking of the models showed differences for each metric. The results shown in Appendix A are based upon the JEA source term. The comparison of results presented in Tables 5, 6, and Appendix A also illustrates the variability introduced by the assumptions regarding the time variation of the source strengths. For example, the revised JMA-MESO-R results (for Cs-137 ground deposition) using the JAEA source term had a Rank value of 3.28, compared to the Rank value 2.94 using the UNSCEAR source

term. To illustrate sensitivity to changes in model parameterizations, the original JMA-MESO-R calculation showed a Rank value of 3.22 with the JAEA source term, and 2.89 using UNSCEAR source information.

Because of the uncertainty in determining the best meteorology and implicitly ATDM combination, another approach is to compute a mean of all the results. Out of the 18 ATDM-meteorology combinations shown in Table 3, ten were selected to represent each ATDM and most of the meteorological analyses. When there were several possibilities for an ATDM-meteorology combination, the tendency was to select the calculation with the highest Rank, except when that meteorological analysis was already over-represented by one of the other ATDMs. The combinations selected for the ensemble are shown in bold in Table 5. Each ATDM is represented by two meteorological analyses. The MESO, ECMWF, GDAS, and GEM analyses are represented by four, three, two, and one member, respectively. Out of these ten, three meteorological analyses used the RAP for the wet deposition calculations. The mean model results of the ten members are identified in Table 5 by the designation ENS-select, while the mean of all the members is identified by ENS-all. In general the performance statistics between all the members and the select ten is comparable, with the ten showing slightly better results. No doubt it is possible to select a group of models that will maximize a given deposition performance metric and this will be discussed in more detail in Section 10. However, as will be shown in the next section, it is also necessary to consider the performance of the models' air concentration predictions.

An example of the computed Cs-137 deposition pattern for the ENS-MEAN model (select ten) is shown in Figure 8 which can be directly compared with the measured deposition pattern shown in Figure 5. The computed high deposition region shows a comparable downwind direction to the measurements, including the turn to the southwest, less transport to the north, and a much smoother pattern, more consistent with the measurements.

Another quantitative comparison would be the deposition scatter diagram shown in Fig 9 for the mean model (A) and the highest ranking model (B), for each of the measured deposition data grid points. This more clearly illustrates a slight under-prediction for the highest measured depositions and an over-prediction for the lower deposition measurements. The scatter diagram shows that the level of uncertainty for any one measurement is about a factor of 10. In contrast, the best model (highest rank) shows much more scatter at the lower range of measured deposition. The ensemble model shows a much tighter scatter pattern than the best model, illustrating the advantage of using an ensemble model product rather than a single model for subsequent assessment calculations and not relying upon a single metric for evaluating model results.

9.2 Air Concentration

Only two locations that collected radionuclide air concentration data were available to the TT. These two sites were located at the periphery of the main transport corridor. As noted earlier, one site was contaminated and therefore we only examined the time series data at one location, JAEA, about 110 km south of the accident site for the same ATDM-meteorological combinations shown for the deposition patterns. Model performance for air concentrations is a critical part of the dose calculation. The statistical results for the JAEA sampling site are summarized in Table 6. In terms of overall rank, the best ATDM-meteorology combination is no longer NOAA-ECMWF, as was the case for deposition, but the CMC-MESO combination, followed by the revised JMA-MESO, and then the ENS-select result. The results are only for one location and there are only 41 temporal values compared with the 543 deposition grid points. However, the results are suggestive of the difficulty in assigning a single metric for evaluation purposes.

The quality of the air concentration calculations as compared to the deposition calculation is best illustrated qualitatively by examining the time series of calculated and measured air concentrations at the JAEA sampling site using the same ATDM-meteorology combinations shown in the deposition section. The NOAA ATDM

calculation using ECMWF and MESO data is shown in Figure 10. The results are qualitatively consistent with the NOAA deposition statistics, in that the calculation using the MESO data is more variable and not as good as the calculation using the ECMWF analysis. It is interesting to note that this is the only model that showed a poorer performance using the MESO data compared with the global data, suggesting the importance of how the model incorporates higher resolution data into its computational framework, especially the vertical motion component of the calculation.

In contrast, the comparable calculation using the UKMET ATDM shows (Figure 11) quite good performance with the ECMWF data (rank=1.80) and even better performance using the MESO data (rank=2.12). The more complex and granular spatial deposition pattern shown by the NOAA model did not translate into a better prediction of the air concentration time series. The inclusion of the MESO data resulted in a prediction of the second peak on the 15th as well as capturing the last peak toward the end of the month.

The ensemble mean calculation in this case is better (Rank=2.22) than all the other ATDM-meteorology combinations except the CMC ATDM (Rank=2.52) and the revised JMA-MESO (Rank=2.38). However, examining the two time series (Figure 12) doesn't show any systematic differences between the ENS and CMC simulations, suggesting that the small differences in the quantitative statistics are irrelevant.

10 Further Ensemble Analysis

The previous ten member ensemble model results were provided to UNSCEAR for their dose assessment study. Subsequently, additional analyses of the model results using the latest developments in ensemble treatment, has led to alternative pathways with respect to the selection of the members as described below.

As demonstrated in the past (Potempski and Galmarini, 2009), a multi-model (MM) analysis has to consider the fact that models are not independent, sharing large portions of their modules. A MM ensemble may therefore be characterized by overlaps which do not cancel out and may produce a serious deterioration of the ensemble performance (Solazzo et al., 2012). Simplistic statistical treatments of model results (a simple MM average, for example) can be deceiving and lead to incorrect conclusions.

The aim of the analysis in this section is to assess the ensemble of TT models in order to identify the original, non-repetitive contribution each model brings to the ensemble. To this scope we need to identify and remove unnecessary model overlaps. We consider the 18 model predictions of Cs-137 deposition at 543 receptors in the Fukushima region as described in this report (excluding the recently revised JMA-RATM results).

As it is not practical to assess the independence of models and their results, we focus on:

- a) Identifying to what extent the combination of all 18 model results is meaningful with respect to the observed variability;
- b) Having assessed that, to use the currently available theoretical analysis to identify the subset of models out of the 18 available that provides non-redundant information;
- c) To use a heuristic approach to verify the consistency with the theory and to identify and characterize the members of the subset.

10.1 Redundancy of dataset

When projecting the observation anomalies ($\text{obs} - \text{mean}(\text{obs})$) onto the principal components (PCs) of the covariance matrix of the deviation of the ensemble of models from the MM mean, we find that the first (largest) eigenvalue already accounts for more than twice the observed spatial variability. Moreover, when all eigenvalues are taken into account, the MM mean can explain approximately 9 times the observed variability for deposited Cs-137. According to the definition of Annan and Hargreaves (2010) the ensemble is therefore *wide*. Dealing with a wide ensemble implies that there is a substantial amount of redundant variability that is variability already accounted for by other models. One consequence of this is that the ensemble size is simply too large and not all information contained is needed in principle. In particular that would be the case if the presence of redundant information were to produce a deterioration of the ensemble result as investigated in the next section.

10.2 Data reduction

Following Bretherton et al (1999) and Pennel and Reichler (2011), we calculate the number of effective models (M_{eff}) sufficient to reproduce the variability of the full ensemble. Under the assumption that the modelled and observed fields are normally distributed, the fraction of the overall variance expressed by the first M_{eff} eigenvalues is 86% (Equation 8 of Bretherton et al., 1999). By construction, $M_{\text{eff}} = M$ only if all eigenvalues were equal to unity, which corresponds to the situation in which all directions are equally important. On the other hand, if all error fields were similar, only one eigenvalue would be non-zero and $M_{\text{eff}} = 1$. Thus, we can think of replicating the full variability of the M -members by a M_{eff} -dimensional subset of these in a vector space whose base is generated by the eigenvectors of the largest eigenvalues. As noted by Pennel and Reichler (2011), the concavity of the M_{eff} plot as a function of the number of models presented. Figure 13 indicates that the addition of more models to the ensemble is not compensated for by a linear increase in the overall information. This is a direct consequence of commonalities among members. In other words the chance that a new member shares features with another one increases as the ensemble size does. This would not happen in the case of totally independent models.

10.3 Reduced MM ensemble

We now explore a heuristic data-reduction technique, which allows *i)* the identifying the dimensionality of the subspace, and *ii)* selecting the members to generate skilful but reduced ensembles. In Figure 14 we report, for all possible subsets of ensembles generated with the available pool of models, the curves of the most skilful ensembles. The identification of the reduced set was based on the same statistical metrics use for the evaluation of the individual model performance as previously shown. The top-left panel shows the curve of minimum RMSE, then clockwise the maximum Rank (M1), the maximum PCC and finally the minimum FB. For all metrics there exists a subset of models whose ensemble mean largely outscore the full ensemble mean. For example, the minimum RMSE obtained by combining five members is ~30% lower than the 18-member ensemble. This is an indication of the deterioration of the skills of the ensemble when more redundant members are combined depending on the fact that the contributions are not independent, model differences (errors) are not random and they do not cancel out. The curves shown in Figure 14 represent the best performing groups as a function of the number of members. For each metric, results are reported in Table 7.

The PCC and RMSE identify the same models. We have scored the reduced ensemble against all of the other metrics plus the variability, measured by the standard deviation (Table 8 - ratio of the standard deviation of the ensemble to that of the measurements). The combination of model results with the min RMSE has the best accuracy (minimum error, by definition) and also records the standard deviation closest to the standard deviation of the measurements. For this reason we retain the combination of the five models: NOAA-GDAS; UKMET-MESO; UKMET-ECMWF; NOAA-ECMWF; ZAMG-ECMWF, as the best possible subset.

The dimension of the previously noted five member subset is in perfect agreement with the analysis of *Meff*, indicating that this is indeed the level of diversity that is possible to express out of the available dataset. In Table 8, along with the members, we report the score of each individual member for that particular metric. In the case of RMSE, the best subset is generated by the top five scoring models, i.e. the models that, individually, perform among the best five. In general, this is not always the case. On the contrary, it is more common to deal with subsets of mix-ranked members in light of the redundancy of the members (e.g. Solazzo et al., 2012). The fact that the first ranked models are also those whose mean minimizes the error is an indication that these models are poorly correlated. In fact, if two best features depend heavily on one another, we can observe some large correlation between the two then conceptually one contains some of the information of the other. This means that when considering the two together as a predictor we get very little decrease in error compared to either single one of the two. The result obtained both with the theoretical analysis and the heuristic approach can also be seen from the clustering of the members. In Figure15, the association is based on the matrix of correlations from which the eigenvalues were derived. Four out of the five models belong to different clusters (arrows). NOAA-GDAS and UKMET-MESO, although not strictly correlated (level of dissimilarity ~ 0.6), share some similarities and belong to the same cluster. UKMET-ECMWF, other than being high-ranked (4th) has the highest level of diversity and is not grouped to any other model. Note that the first branch of the dendrogram (NOAA-MESO-RAP, NOAA-MESO) is the most redundant one as it shares the largest portion of commonalities with the other cluster, and is not represented in the selected quintuplet.

10.4 Relaxation of the set reduction

The answers to the original research items are therefore:

- a) The variability of the ensemble mean of the 18 models covers 9 times the observed variability and is therefore redundant; the use of all results may produce a deteriorated and statistically biased result.
- b) The identified optimal subset corresponds to 4 or 5 models out of 18. Any other model added beyond this number deteriorates the ensemble RMSE.
- c) A subset of 5 models was identified namely: NOAA-GDAS, UKMET-MESO, UKMET-ECMWF, NOAA-ECMWF, and ZAMG-ECMWF. It was shown that the five are representatives of four independent correlation clusters thus corroborating the finding that their contribution is original and improves the ensemble result.

Additionally it is important to note that:

- a) The heuristic analysis performed is case-specific and metric-specific.
- b) The identification of a minimum subset does not imply, unless evidence is presented, that the number of models and the selected members will be the same in other cases.
- c) The identification of an optimum subset requires that a large pool of appropriate model results be available.

d) In general, an analysis of the ensemble optimum subsets is strongly recommended as the use of all model results can lead to a deterioration of the ensemble outcome.

The ten member ensemble was compared with the minimum set and two alternatives (Table 9). The compared performance of all models is presented in Figure 16. In the figure we show in addition to the minimum set (magenta square) and the ten member ensemble (black square), set #1 (red square) made of five members by substituting UK-MET-MESO with CMC-MESO as described above as a possible alternative and NOAA-ECMWF with JMA's MESO-RAP; set #2 (blue square) containing at least one representative per group.

The figure clearly shows that set #1 and #2 cluster close to the minimum set values while the 10 member set tends to have a performance close to the average of the possible combinations of 10 members. An aspect that will require a deeper analysis relates to understanding the extent to which the differences outlined in the figure are producing significant effects in terms of the spatial distribution and the final dose assessment, given the inherent uncertainties contained in the calculation procedure and measurements.

11 Model Uncertainties

The previous deposition results only showed the mean model performance with respect to the measurements over the whole domain. To get a sense of the range of the individual member predictions composing the mean model, probability deposition box plots are shown in Figure 17 at five locations computed according to the procedure described by Draxler (2001). Here the deposition measurement is represented by the red "X" and quartiles by the box and the deciles by the whiskers. Because the ensemble is comprised of only 10 members, the 5th and 95th percentile values (o) are identical to the decile values. In the town of Fukushima, the measurement falls just below the median prediction (centre line), the mean prediction (+) is much higher than the median just above the upper quartile, and the overall range is about a factor of 10. At Iitate, the measurement is near the 90th percentile value, while at Sendai, the measurement falls near the lower quartile. At the locations where measured deposition was available, the measurements fall within the range of the ATDM predictions.

The uncertainty of the air concentration time series predictions at these locations can be illustrated by showing the ATDM-meteorology variance with each prediction. The variance is computed from

$$V = \frac{\sum (P_i - \bar{P})^2}{N}$$

where V is the variance and P represents difference of the model prediction for each of N members from the mean. The results at Fukushima are shown in Figure 18 for the Cs-137 air concentration time series. The black circles represent the model calculations while the variance is shown in red (units = concentration²). For instance, the peak predicted concentration on the 15th is just over 10⁵ mBq m⁻³ while the variance is just over (10⁸ mBq m⁻³)² or 10⁴ mBq m⁻³. In contrast, the rather low predicted peak on the 28th has an even lower variance, essentially suggesting that none of the ensemble members showed any large prediction at that time. In general the ensemble ATDM predictions are skewed toward zero because several members may make no contribution, a situation where the transport is not over the sampler, while the peak concentrations will be limited by the emissions and a minimal dispersion factor when the radionuclide plume is directly over the location of interest.

The air concentration/variance time series at the four other locations is shown in Figure 19. These plots are intended as a quick visual reference to see if the concentration uncertainty is consistent between different time

periods and locations. For instance, at Iitate the variance values at the time of the air concentration peaks are consistently larger than the air concentrations, while at Sendai, only a few of the peaks show a higher variance.

12 Summary and conclusions

The previous sections discussed the overall methodology in developing various ATDM-meteorology calculations and evaluating the model results. Naturally the results are quite dependent upon the magnitude of the time-varying source term and these results may change in the future as more knowledge about the emissions becomes available. Due to the nature of the ATDM computational framework, the dispersion and deposition calculations do not have to be re-run, but the existing unit source calculations can be adjusted to reflect the updated source term. The ATDM results with interactive source term adjustments and the computation of statistical performance measures, is available for all the ATDM calculations at the previously cited URL (http://ready.arl.noaa.gov/READY_fdnpwmo.php).

Five WMO TT members provided computational results for 20 ATDM-meteorology combinations. Some of the best deposition results were obtained from ATDM's that used the highest spatial and temporal resolution meteorological fields. This was also true for the case of air concentrations for the limited measured data available to the TT in the evaluation. However, the conclusion is not simply that the highest resolution data provided the best results. For example, additional uncertainty and variability may have been introduced into the calculations because a certain amount of pre-processing was required for each of the ATDM's to effectively deal with different meteorological input data sets.

In general, the individual ATDM results tended to improve when the MESO analysis was used instead of global analyses. This was particularly the case for the air concentration results. It was also observed that the use of the RAP data as input to the models in place of the NWP precipitation fields resulted in a deterioration of ATDM results (see last table of Summary and Discussion of Appendix A). The reason for that is currently unknown.

Effectively the same ATDM-meteorology combination may not be the best at all locations and time periods. To address this issue, the TT provided an ensemble mean calculation for the best 10 ATDM-meteorology combinations available at the time the calculations were required by UNSCEAR. This approach provides for the computation of uncertainties associated with the model predictions. Subsequently, additional analyses based on the independence of the ATDM results showed that the ensemble model performance for deposition could be improved by selecting different subsets of members depending upon their skill. However, as highlighted in section 10, the identification of alternative subsets does not imply that the number of models and the selected members will be the same in other cases. In fact, the identification of an optimum subset requires a large pool of model results to be available. Further investigation will be required to assess the effect of the different ensembles on the final result. The uncertainty chain that connects a deposition assessment to a dose might overshadow the differences in the performance of various ensembles.

13 Acknowledgements

We thank Masamichi Chino from the Japan Atomic Energy Agency for providing source term and air concentration measurement data; Florian Gering from the Bundesamt für Strahlenschutz (BfS) for providing us the digitized MEXT Cs-137 deposition measurements; Petra Seibert from the University of Vienna for providing modifications of the FLEXPART wet deposition scheme; Teruki Kato of the Meteorological Research Institute of Japan and Tabito Hara of the Japan Meteorological Agency for providing JMA-MESO and -RAP analyses and their file converter kit; the European Centre For Medium-Range Weather Forecasts (ECMWF) at Shinfield Park, Reading, RG2 9AX, United Kingdom for making their meteorological data analysis available, and Peter

Chen and Alice Soares of the WMO Secretariat for taking the initiative to organize the effort to assist the UNSCEAR assessment and organizing the Task Team activities.

14 References

- Annan, J.D. and J.C. Hargreaves, 2010, Reliability of the CMIP3 ensemble, *Geophysical Research Letters*, **37**, L02703
- Becker, A. *et al.*, 2007, Global backtracking of anthropogenic radionuclides by means of a receptor oriented ensemble dispersion modelling system in support of Nuclear-Test-Ban Treaty verification. *Atmospheric Environment* **41**, 4520–4534, [doi:10.1016/j.atmosenv.2006.12.048](https://doi.org/10.1016/j.atmosenv.2006.12.048).
- Bedwell, P., J. Wellings, S.M. Haywood, A.R. Jones, M.C. Hort, 2011, Cloud Gamma Modelling in the UK Met Office's NAME III Model, *AGU Chapman Conference*.
- Bélair, S., M. Roch, A.-M. Leduc, P. A. Vaillancourt, S. Laroche, J. Mailhot, 2009, Medium-Range Quantitative Precipitation Forecasts from Canada's New 33-km Deterministic Global Operational System, *Weather and Forecasting*, **24**, 690–708, [doi:10.1175/2008WAF2222175.1](https://doi.org/10.1175/2008WAF2222175.1).
- Bretherton, C.S., M. Widman, V.P. Dymnikov, J.M. Wallace, I. Bladè, 1999, The effective number of spatial degrees of freedom of a time-varying field, *J. Climate*, **12**, 1990–2009.
- Brioude, J., *et al.*, 2011, Top-down estimate of anthropogenic emission inventories and their interannual variability in Houston using a mesoscale inverse modeling technique, *Journal of Geophysical Research*, **116** (D20305), [doi:10.1029/2011JD016215](https://doi.org/10.1029/2011JD016215).
- Brioude, J., W.M. Angevine, S.A. McKeen, E.-Y. Hsieh, 2012, Numerical uncertainty at mesoscale in a Lagrangian model in complex terrain, *Geoscientific Model Development*, **5**, 1127–1136, [doi:10.5194/gmd-5-1127-2012](https://doi.org/10.5194/gmd-5-1127-2012).
- Burgin, L.E., J. Gloster, C. Sanders, P.S. Mellor, S. Gubbins, S. Carpenter, 2012, Investigating Incursions of Bluetongue Virus Using a Model of Long-Distance Culicoides Biting Midge Dispersal, *Transboundary and Emerging Diseases*, [doi:10.1111/j.1865-1682.2012.01345.x](https://doi.org/10.1111/j.1865-1682.2012.01345.x).
- Byun, D. and K. L. Schere, 2006, Review of the Governing Equations, Computational Algorithms, and Other Components of the Models-3 Community Multiscale Air Quality (CMAQ) Modeling System, *Applied Mechanics Reviews*, **59**, 51–77, [doi:10.1115/1.2128636](https://doi.org/10.1115/1.2128636).
- Chang, J.C. and S.R. Hanna, 2004, Air quality model performance evaluation, *Meteorology Atmospheric Physics*, **87**, 167–196, [doi:10.1007/s00703-003-0070-7](https://doi.org/10.1007/s00703-003-0070-7).
- Charron, M., S. Polavarapu, M. Buehner, P. A. Vaillancourt, C. Charette, M. Roch, J. Morneau, L. Garand, J. M. Aparicio, S. MacPherson, S. Pellerin, J. St-James, and S. Heilliette, 2012, The Stratospheric Extension of the Canadian Global Deterministic Medium-Range Weather Forecasting System and Its Impact on Tropospheric Forecasts, *Monthly Weather Review*, **140**, 1924–1944, [doi:10.1175/MWR-D-11-00097.1](https://doi.org/10.1175/MWR-D-11-00097.1).
- Chino, M., H. Nakayama, H. Nagai, H. Terada, G. Katata, and H. Yamazawa, 2011, Preliminary Estimation of Release Amounts of ¹³¹I and ¹³⁷Cs Accidentally Discharged from the Fukushima Daiichi Nuclear Power Plant into the Atmosphere, *Journal of Nuclear Science and Technology*, **48**, 1129–1134, [doi:10.1080/18811248.2011.9711799](https://doi.org/10.1080/18811248.2011.9711799).

- Chino, M., 2012, Air concentration measurements at the Japan Atomic Energy Agency, private communication.
- CMC, 2009, A new stratosphere-troposphere assimilation and medium range forecast system for operational numerical weather prediction, *Environment Canada's Technical Notes on Operational Implementations*, http://collaboration.cmc.ec.gc.ca/cmc/cmci/product_guide/docs/lib/op_systems/doc_opchanges/technote_glbstrato_20090618_en.pdf.
- CMC, 2012, Improvements to the Regional Deterministic Prediction System (RDPS) from version 2.0.0 to version 3.0.0, *Environment Canada's Technical Notes on Operational Implementations*, 76 pp., http://collaboration.cmc.ec.gc.ca/cmc/cmci/product_guide/docs/lib/op_systems/doc_opchanges/technote_rdps_20121003_e.pdf.
- Cohen, M., R. Draxler, R. Artz, et al., 2002, Modeling the Atmospheric Transport and Deposition of PCDD/F to the Great Lakes, *Environmental Science & Technology*, **36**, 4831–4845, [doi:10.1021/es0157292](https://doi.org/10.1021/es0157292).
- Côté, J., S. Gravel, A. Méthot, A. Patoine, M. Roch, A. Staniforth, 1998, The Operational CMC–MRB Global Environmental Multiscale (GEM) Model, Part I: Design Considerations and Formulation, *Monthly Weather Review*, **126**, 1373–1395, [doi:10.1175/1520-0493\(1998\)126<1373:TOCMGE>2.0.CO;2](https://doi.org/10.1175/1520-0493(1998)126<1373:TOCMGE>2.0.CO;2).
- Côté, J., J.-G. Desmarais, S. Gravel, A. Méthot, A. Patoine, M. Roch, A. Staniforth, 1998, The Operational CMC–MRB Global Environmental Multiscale (GEM) Model. Part II: Results, *Monthly Weather Review*, **126**, 1397–1418, [doi:10.1175/1520-0493\(1998\)126<1397:TOCMGE>2.0.CO;2](https://doi.org/10.1175/1520-0493(1998)126<1397:TOCMGE>2.0.CO;2).
- D'Amours, R. and A. Malo, 2004, A Zeroth Order Lagrangian Particle Dispersion Model MLDP0, *Internal Publication, Canadian Meteorological Centre, Environmental Emergency Response Section*, Dorval, QC, Canada, 19 pp, <http://eer.cmc.ec.gc.ca/publications/DAmours.Malo.2004.CMC-EER.MLDP0.pdf>.
- D'Amours, R., A. Malo, R. Servranckx, D. Bensimon, S. Trudel, J.-P. Gauthier, 2010, Application of the atmospheric Lagrangian particle dispersion model MLDP0 to the 2008 eruptions of Okmok and Kasatochi volcanoes, *J. Geophys. Res.*, **115** (D00L11), 11pp, [doi:10.1029/2009JD013602](https://doi.org/10.1029/2009JD013602).
- Davies, T., M.J.P. Cullen, A.J. Malcolm, M.H. Mawson, A. Staniforth, A.A. White, N. Wood, 2005, A new dynamical core for the Met Office's global and regional modelling of the atmosphere. *Q.J.R. Meteorol. Soc.*, **131**: 1759–1782, [doi: 10.1256/qj.04.101](https://doi.org/10.1256/qj.04.101).
- Delage, Y., 1997, Parameterising Sub-Grid Scale Vertical Transport in Atmospheric Models Under Statically Stable Conditions, *Boundary-Layer Meteorology*, **82**, 23–48, [doi:10.1023/A:1000132524077](https://doi.org/10.1023/A:1000132524077).
- Draxler, R.R., 2006, The Use of Global and Mesoscale Meteorological Model Data to Predict the Transport and Dispersion of Tracer Plumes over Washington, D.C, *Weather and Forecasting*, **21**, 383–394, [doi:10.1175/WAF926.1](https://doi.org/10.1175/WAF926.1).
- Draxler, R.R., 2001, Evaluation of an ensemble dispersion calculation, *J. Appl. Meteorol.*, **42**, 308-317.
- Draxler, R.R., 1999, HYSPLIT_4 User's Guide, NOAA Tech. Memo, ERL ARL-230, Air Resources Laboratory, Silver Spring, MD, 35 p., http://www.arl.noaa.gov/documents/reports/hysplit_user_guide.pdf.
- Draxler, R.R. and G.D. Hess, 1998, An overview of the HYSPLIT_4 modelling system for trajectories, dispersion, and deposition, *Australian Meteorological Magazine*, **47**, 295–308.
- Draxler, R.R. and G.D. Hess, 1997, Description of the HYSPLIT_4 modeling system, NOAA Tech. Memo. ERL ARL-224, Air Resources Laboratory, Silver Spring, MD, 24 p., [NTIS PB98-116593](https://www.ntis.gov/pubnum/?PB98-116593).

- Draxler, R.R. and G.D. Rolph, 2012, Evaluation of the Transfer Coefficient Matrix (TCM) approach to model the atmospheric radionuclide air concentrations from Fukushima, *Journal of Geophysical Research*, **117** (D05107), [doi:10.1029/2011JD017205](https://doi.org/10.1029/2011JD017205).
- ECMWF, 1995, User guide to ECMWF products 2.1, Meteorological Bulletin M3.2, ECMWF, Reading, UK.
- Fast, J., and R. Easter, 2006, A Lagrangian particle dispersion model compatible with WRF, in: 7th WRF Users Workshop, NCAR, June 19-22, Boulder, Colorado.
- Fillion, L., M. Tanguay, E. Lapalme, B. Denis, M. Desgagné, V. Lee, N. Ek, Z. Liu, M. Lajoie, J.-F. Caron, C. Pagé, 2010, The Canadian Regional Data Assimilation and Forecasting System, *Weather and Forecasting*, **25**, 1645–1669, [doi:10.1175/2010WAF2222401.1](https://doi.org/10.1175/2010WAF2222401.1).
- Fischer, B., 2012, Radionuclide emissions for the Fukushima Daiichi accident prepared for the UNSCEAR assessment, private communication.
- Forster, C., A. Stohl, P. Seibert, 2007, Parameterization of Convective Transport in a Lagrangian Particle Dispersion Model and Its Evaluation, *Journal of Applied Meteorology and Climatology*, **46**, 403–422, [doi:10.1175/JAM2470.1](https://doi.org/10.1175/JAM2470.1).
- Fox, D.G., 1984, Uncertainty in air quality modeling, *Bulletin of the American Meteorology Society*, **65**, 27–36, [doi:10.1175/1520-0477\(1984\)065<0027:UIAQM>2.0.CO;2](https://doi.org/10.1175/1520-0477(1984)065<0027:UIAQM>2.0.CO;2).
- Furuta, S., S. Sumiya, H. Watanabe, M. Nakano, K. Imaizumi, M. Takeyasu, A. Nakada, H. Fujita, T. Mizutani, M. Morisawa, Y. Kokubun, T. Kono, M. Nagaoka, H. Yokoyama, T. Hokama, T. Isozaki, M. Nemota, Y. Hiyama, T. Onuma, C. Kato, and T. Kurachi, 2011, Results of the Environmental Radiation Monitoring Following the Accident at the Fukushima Daiichi Nuclear Power Plant - Interim Report (Ambient Radiation Dose Rate, Radioactivity Concentration in the Air and Radioactivity Concentration in the Fallout), Radiation Protection Department, Nuclear Fuel Cycle Engineering Laboratories, Tokai Research and Development Center, Japan Atomic Energy Agency Tokai-mura, Naka-gun, Ibaraki-ken, JAEA-Review 2011-035, August, 90 p. (in Japanese)
- Gauthier, P., M. Tanguay, S. Laroche, S. Pellerin, J. Morneau, 2007, Extension of 3DVAR to 4DVAR: Implementation of 4DVAR at the Meteorological Service of Canada, *Monthly Weather Review*, **135**, 2339–2354, [doi:10.1175/MWR3394.1](https://doi.org/10.1175/MWR3394.1).
- Graziani, G., W. Klug, S. Mosca, 1998, Real-time long-range dispersion model evaluation of the ETEX first release, Joint Research Centre, European Commission, EUR-17754, ISBN 92-828-3657-6, 216 pp. [Available from the Office for Official Publications of the European Communities, Luxembourg.]
- Hanna, S.R., 1989, Confidence limits for air quality model evaluations, as estimated by bootstrap and jackknife resampling methods, *Atmos. Environ.*, **23**, 1385–1398, [doi:10.1016/0004-6981\(89\)90161-3](https://doi.org/10.1016/0004-6981(89)90161-3).
- Hanna, S.R., 1993, Uncertainties in air quality model predictions, *Boundary-Layer Meteorology*, **62**, 3–20, [doi:10.1007/BF00705545](https://doi.org/10.1007/BF00705545).
- Heard, I.P.C., A.J. Manning, J.M. Haywood, C. Witham, A. Redington, A. Jones, L. Clarisse, and A. Bourassa, 2012, A comparison of atmospheric dispersion model predictions with observations of SO₂ and sulphate aerosol from volcanic eruptions, *J. Geophys. Res.*, **117** (D00U22), [doi:10.1029/2011JD016791](https://doi.org/10.1029/2011JD016791).

- Hertel, O., J. Christensen, E.H. Runge, W.A.H Asman, R. Berkowicz, M.F. Hovmand and O. Hov, 1995, Development and testing of a new variable scale air pollution model—ACDEP, *Atmos. Environ.*, **29**, 1267–1290, [doi:10.1016/1352-2310\(95\)00067-9](https://doi.org/10.1016/1352-2310(95)00067-9).
- Hicks, B.B., 1986, Differences in wet and dry particle deposition parameters between North America and Europe, *Aerosols: Research, Risk Assessment, and Control Strategies*, Lewis Publishers, Chelsea, MI, 973–982.
- Honda, Y., M. Nishijima, K. Koizumi, Y. Ohta, K. Tamiya, T. Kawabata, T. Tsuyuki, 2005, A pre-operational variational data assimilation system for a non-hydrostatic model at the Japan Meteorological Agency: formulation and preliminary results, *Q. J. Roy. Met. Soc.*, **131**, 3465–3475, [doi:10.1256/qj.05.132](https://doi.org/10.1256/qj.05.132).
- Honda, Y. and K. Sawada, 2008, A new 4D-Var for mesoscale analysis at the Japan Meteorological Agency, *CAS/JSC WGNE, Res. Act. Atmos. Ocea. Model*, **38**, 01.7–01.8.
- Jones, A.R., D.J. Thomson, M.C. Hort, B. Devenish, 2007, The U.K. Met Office's next-generation atmospheric dispersion model, NAME III. In C Borrego and A L Norman, editors, *Air Pollution and its Applications XVII (Proceedings of the 27th NATO/CCMS International Technical Meeting on Air Pollution Modelling and its Application*, pages 580-589. Springer.
- Iwasaki, T., T. Maki, K. Katayama, 1998, Tracer transport model at Japan Meteorological Agency and its application to the ETEX data, *Atmos. Environ.*, **32**, 4285–4295, [doi:10.1016/S1352-2310\(98\)00171-X](https://doi.org/10.1016/S1352-2310(98)00171-X).
- Katata, G., H. Terada, H. Nagai, and M. Chino, 2012, Numerical reconstruction of high dose rate zones due to the Fukushima Dai-ichi Nuclear Power Plant accident, *Journal of Environmental Radioactivity*, **111**, [doi:10.1016/j.jenvrad.2011.09.011](https://doi.org/10.1016/j.jenvrad.2011.09.011).
- Kitada, T., 1994, Modelling of transport, reaction and deposition of acid rain, *Kishou Kenkyu Note*, **182**, 95–117. (in Japanese)
- Korsakissok, I., D. Didier, A. Mathieu, D. Quelo, J. Groell, E. Quentric, M. Tombette, J.P. Benoit, and O. Saunier, 2011, Evaluation of the atmospheric releases of the Fukushima accident and their consequences, Institut de Radioprotection et de Sûreté Nucléaire (IRSN), PRP-CRI/SESUC n° 2011-00299, 38 p.
- Kanamitsu, M., 1989, Description of the NMC global data assimilation and forecast system, *Weather and Forecasting*, **4**, 335–342, [doi:10.1175/1520-0434\(1989\)004<0335:DOTNGD>2.0.CO;2](https://doi.org/10.1175/1520-0434(1989)004<0335:DOTNGD>2.0.CO;2).
- Kanamitsu, M., J.C. Alpert, K.A. Campana, P.M. Caplan, D.G. Deaven, M. Iredell, B. Katz, H.-L. Pan, J. Sela, G. H. White, 1991, Recent changes implemented into the global forecast system at NMC, *Weather and Forecasting*, **6**, 425–435, [doi:10.1175/1520-0434\(1991\)006<0425:RCIITG>2.0.CO;2](https://doi.org/10.1175/1520-0434(1991)006<0425:RCIITG>2.0.CO;2).
- Kinoshita, N., K. Sueki, K. Sasa, J.-I. Kitagawa, S. Ikarashi, T. Nishimura, Y.-S. Wong, Y. Satou, K. Handa, T. Takahashi, M. Sato, T. Yamagata, 2011, Assessment of individual radionuclide distributions from the Fukushima nuclear accident covering central-east Japan, *Proceedings of the National Academy of Sciences of the United States of America*, 4pp, www.pnas.org/cgi/doi/10.1073/pnas.1111724108[doi:10.1073/pnas.1111724108](https://doi.org/10.1073/pnas.1111724108).
- Laroche, S., P. Gauthier, M. Tanguay, S. Pellerin, and J. Morneau, 2007, Impact of the Different Components of 4DVAR on the Global Forecast System of the Meteorological Service of Canada, *Monthly Weather Review*, **135**, 2355–2364, [doi:10.1175/MWR3408.1](https://doi.org/10.1175/MWR3408.1).

- Mailhot, J., S. Bélair, L. Lefaivre, B. Bilodeau, M. Desgagné, C. Girard, A. Glazer, A.-M. Leduc, A. Méthot, A. Patoine, A. Plante, A. Rahill, T. Robinson, D. Talbot, A. Tremblay, P. Vaillancourt, A. Zadra, A. Qaddouri, 2006, The 15-km Version of the Canadian Regional Forecast System, *Atmosphere-Ocean*, **44**, 133–149, [doi:10.3137/ao.440202](https://doi.org/10.3137/ao.440202).
- Manning, A.J., S. O'Doherty, A.R. Jones, P.G. Simmonds, R.G. Derwent, 2011. Estimating UK methane and nitrous oxide emissions from 1990 to 2007 using an inversion modeling approach. *J. of Geophys. Res.* **116**, [doi:10.1029/2010JD014763](https://doi.org/10.1029/2010JD014763).
- McMahon, T.A., P.J. Denison, 1979, Empirical atmospheric deposition parameters—A survey, *Atmospheric Environment*, **13**, 571–585, [doi:10.1016/0004-6981\(79\)90186-0](https://doi.org/10.1016/0004-6981(79)90186-0).
- Maryon, R.H., D.B. Ryall and A.L. Malcolm, 1999, The NAME 4 dispersion model: Science documentation. Technical report, UK Meteorological Office. Turbulence Diffusion Note No. 262.
- MEXT, 2011, http://www.mext.go.jp/b_menu/shingji/chousa/gijyutu/017/shiryo/_icsFiles/afieldfile/2011/09/02/1310688_1.pdf
- Mahfouf, J.-F. and F. Rabier, 2000, The ECMWF operational implementation of four-dimensional variational assimilation. II: Experimental results with improved physics. *Q.J.R. Meteorol. Soc.*, **126**, 1171–1190, [doi:10.1002/qj.49712656416](https://doi.org/10.1002/qj.49712656416).
- Morino, Y., T. Ohara, M. Nishizawa, 2011, Atmospheric behavior, deposition, and budget of radioactive materials from the Fukushima Daiichi nuclear power plant in March 2011, *Geophysical Research Letters*, **38** (L00G11), [doi:10.1029/2011GL048689](https://doi.org/10.1029/2011GL048689).
- Mosca, S., G. Graziani, W. Klug, R. Bellasio, R. Bianconi, 1998, A statistical methodology for the evaluation of long-range dispersion models: an application to the ETEX exercise, *Atmospheric Environment*, **32**, 4307–4324, [doi:10.1016/S1352-2310\(98\)00179-4](https://doi.org/10.1016/S1352-2310(98)00179-4).
- Nagata, K., 2011, Quantitative Precipitation Estimation and Quantitative Precipitation Forecasting by the Japan Meteorological Agency, RSMC Tokyo – Typhoon Center Technical Review No.13, 37–50, <http://www.jma.go.jp/jma/jma-eng/jma-center/rsmc-hp-pub-eg/techrev/text13-2.pdf>.
- O'Brien, J.J., 1970, A Note on the Vertical Structure of the Eddy Exchange Coefficient in the Planetary Boundary Layer, *Journal of the Atmospheric Sciences*, **27**, 1213–1215, [doi:10.1175/1520-0469\(1970\)027<1213:ANOTVS>2.0.CO;2](https://doi.org/10.1175/1520-0469(1970)027<1213:ANOTVS>2.0.CO;2).
- Pennel, C. and T. Reichler, 2011. On the effective numbers of climate models, *Journal of Climate*, **24**, 2358–2367.
- Potempski, S. and S. Galmarini, 2009, *Est modus in rebus*: analytical properties of multi-model ensembles, *Atmospheric Chemistry and Physics*, **9**, 9471–9489, [doi:10.5194/acp-9-9471-2009](https://doi.org/10.5194/acp-9-9471-2009).
- Pudykiewicz, J., 1989, Simulation of the Chernobyl dispersion with a 3-D hemispheric tracer model, *Tellus, Series B. Chemical and Physical Meteorology*, **41**, 391–412, [doi:10.1111/j.1600-0889.1989.tb00317.x](https://doi.org/10.1111/j.1600-0889.1989.tb00317.x).
- Rabier, F., H. Järvinen, E. Klinker, J.-F. Mahfouf, A. Simmons, 2000, The ECMWF operational implementation of four-dimensional variational assimilation. I: Experimental results with simplified physics. *Q.J.R. Meteorol. Soc.*, **126**, 1143–1170, [doi:10.1002/qj.49712656415](https://doi.org/10.1002/qj.49712656415).

- Riccio, A., G. Ciaramella, S. Giunta, S. Galmarini, E. Solazzo, S. Potemski, 2012, On the systematic reduction of data complexity in multimodel atmospheric dispersion ensemble modeling, *J. of Geophys. Res.*, **117** (D05314), 12pp, [doi:10.1029/2011JD016503](https://doi.org/10.1029/2011JD016503).
- Ryall, D. B. and R.H. Maryon, 1998. Validation of the UK Met. Office's name model against the ETEX dataset. *Atmospheric Environment*, **32**, 4265–4276, [doi:10.1016/S1352-2310\(98\)00177-0](https://doi.org/10.1016/S1352-2310(98)00177-0).
- Saito, K., J. Ishida, K. Aranami, T. Hara, T. Segawa, M. Narita, Y. Honda, 2007, Nonhydrostatic atmospheric models and operational development at JMA, *Journal of the Meteorological Society of Japan*, **85B**, 271–304, [doi:10.2151/jmsj.85B.271](https://doi.org/10.2151/jmsj.85B.271).
- Saito, K., 2012, The JMA Nonhydrostatic Model and Its Applications to Operation and Research, Atmospheric Model Applications, Ismail Yucel (Ed.), ISBN: 978-953-51-0488-9, InTech, Chapter 5, 85–110, [doi:10.5772/35368](https://doi.org/10.5772/35368).
- Sanson, R., J. Gloster, L. Burgin, 2011, A re-analysis of the start of the United Kingdom 1967-8 foot-and-mouth disease epidemic to calculate airborne transmission probabilities, *Veterinary Record*, **169**, 336-343, [doi:10.1136/vr.d4401](https://doi.org/10.1136/vr.d4401).
- Shimbori, T., Y. Aikawa, K. Fukui, A. Hashimoto, N. Seino, H. Yamasato, 2010, Quantitative tephra fall prediction with the JMA mesoscale tracer transport model for volcanic ash: A case study of the eruption at Asama volcano in 2009, *Pap. Met. Geophys.*, **61**, 13-29, [doi:10.2467/mripapers.61.13](https://doi.org/10.2467/mripapers.61.13).
- Simmons, A.J., D.M. Burridge, M. Jarraud, C. Girard, W. Wergen, 1989, The ECMWF medium-range prediction models: Development of the numerical formulations and the impact of increased resolution. *Meteor. Atmos. Phys.*, **40**, 28–60, [doi:10.1007/BF01027467](https://doi.org/10.1007/BF01027467).
- Skamarock, W.C., J.B. Klemp, J. Dudhia, D.O. Gill, D.M. Barker, M.G. Duda, X.Y. Huang, W. Wang, and J.G. Powers, 2008, A description of the advanced research WRF version 3, NCAR Tech. Note NCAR/TN.475+STR, National Center for Atmospheric Research, Boulder, CO.
- Solazzo, E., R. Bianconi, R. Vautard, W. Appel, M. Moran, et al., 2012, Model evaluation and ensemble modelling of surface-level ozone in Europe and North America in the context of AQMEII, *Atmospheric Environment*, **53**, 60–74, [doi:10.1016/j.atmosenv.2012.01.003](https://doi.org/10.1016/j.atmosenv.2012.01.003).
- Sportisse, B., 2007, A review of parameterizations for modelling dry deposition and scavenging of radionuclides, *Atmos. Environ.*, **41**, 2683-2698, [doi:10.1016/j.atmosenv.2006.11.057](https://doi.org/10.1016/j.atmosenv.2006.11.057).
- Srinivas, C.V., R. Venkatesan, R. Baskaran, V. Rajagopal, B. Venkatraman, 2012, Regional scale atmospheric dispersion simulation of accidental releases of radionuclides from Fukushima Dai-ichi reactor, *Atmos. Environ.*, **61**, 66–84, [doi:http://dx.doi.org/10.1016/j.atmosenv.2012.06.082](http://dx.doi.org/10.1016/j.atmosenv.2012.06.082).
- Stohl, A., C. Forster, A. Frank, P. Seibert, G. Wotawa, 2005, Technical note: The Lagrangian particle dispersion model FLEXPART version 6.2, *Atmospheric Chemistry and Physics*, **5**, 2461-2474, [doi:10.5194/acp-5-2461-2005](https://doi.org/10.5194/acp-5-2461-2005).
- Stohl, A., P. Seibert, G. Wotawa, D. Arnold, J.F. Burkhart, S. Eckhardt, C. Tapia, A. Vargas, and T.J. Yasunari, 2012, Xenon-133 and Caesium-137 releases into the atmosphere from the Fukushima Daiichi nuclear power plant: determination of the source term, atmospheric dispersion, and deposition, *Atmospheric Chemistry and Physics*, **12**, 2313–2343, [doi:10.5194/acp-12-2313-2012](https://doi.org/10.5194/acp-12-2313-2012).

- Stohl, A., M. Hittenberger, and G. Wotawa, 1998, Validation of the Lagrangian particle dispersion model FLEXPART against large-scale tracer experiment data, *Atmos. Environ.*, **32**, 4245–4264, doi:10.1016/S1352-2310(98)00184-8.
- Sugiyama, G., J. Nasstrom, B. Pobanz, K. Foster, M. Simpson, P. Vogt, F. Aluzzi, S. Homann, 2012, Atmospheric dispersion modeling: challenges of the Fukushima Daiichi response, *Health Physics*, **102**, 493–508, doi: 10.1097/HP.0b013e31824c7bc9.
- Takemura, T., H. Nakamura, M. Takigawa, H. Kondo, T. Satomura, T. Miyasaka, T. Nakajima, 2011, A Numerical Simulation of Global Transport of Atmospheric Particles Emitted from the Fukushima Daiichi Nuclear Power Plant, *Scientific Online Letters on the Atmosphere*, **7**, 101–104, doi:10.2151/sola.2011-026.
- Tanguay, M., L. Fillion, E. Lapalme, M. Lajoie, 2012, Four-Dimensional Variational Data Assimilation for the Canadian Regional Deterministic Prediction System, *Monthly Weather Review*, **140**, 1517–1538, doi:10.1175/MWR-D-11-00160.1.
- Terada, H., G. Katata, M. Chino, H. Nagai, 2012, Atmospheric discharge and dispersion of radionuclides during the Fukushima Dai-ichi Nuclear Power Plant accident. Part II: verification of the source term and analysis of regional-scale atmospheric dispersion, *Journal of Environmental Radioactivity*, **112**, 141–154, doi:10.1016/j.jenvrad.2012.05.023.
- USDOE, 2011, United States Department of Energy, <https://explore.data.gov/d/prrn-6s35>.
- Webster, H.N. and D.J. Thomson, 2011, Dry deposition modelling in a Lagrangian dispersion model. *International Journal of Environment and Pollution*, **47**, doi:10.1504/IJEP.2011.047322.
- Webster, H. N. et al., 2012, Operational prediction of ash concentrations in the distal volcanic cloud from the 2010 Eyjafjallajökull eruption, *J. of Geophys. Res.*, **117** (D00U08), 17pp, doi:10.1029/2011JD016790.
- Wilson, J.D., F.J. Ferrandino, G.W. Thurtell, 1989, A Relationship Between Deposition Velocity and Trajectory Reflection Probability for Use in Stochastic Lagrangian Dispersion Models, *Agricultural and Forest Meteorology*, **47**, 139–154, doi:10.1016/0168-1923(89)90092-0.
- Witham, C. and A.J. Manning, 2007, Impacts of Russian biomass burning on UK air quality. *Atmos. Environ.*, **41**, 8075–8090, doi:10.1016/j.atmosenv.2007.06.058.
- WMO, 2011, Final report of the Meeting of the WMO Task Team on Meteorological Analyses for Fukushima Daiichi Nuclear Power Plant Accident, Geneva, Switzerland, 30 November – 2 December 2011, http://www.wmo.int/pages/prog/www/CBS-Reports/documents/FinalRep_TT_FDnpp_v6.pdf.
- WMO, 2012, Final report of the Second Meeting of the WMO Technical Task Team on Meteorological Analyses for Fukushima-Daiichi Nuclear Power Plant Accident, London, UK, 1 – 3 May 2012, www.wmo.int/pages/prog/www/CBS-Reports/documents/FinalReport_TTMetAnalyFDnpp.pdf.

TABLES

Table 1. Summary of the meteorological analysis data used in the ATDM calculations.

Center	CMC	NOAA	ECMWF	UKMET	JMA
Acronym	GEM	GDAS	ECMWF	UKMO	MESO
Domain	Global	Global	Global	Global	Regional
Horizontal	0.3 deg	0.5 deg	0.125 deg	0.23-0.35 deg	5 km
Vertical	58 levels	56 levels	91 levels	70 levels	50 levels
Plane	Eta	Hybrid-P	Hybrid-P	Height	Hybrid-Z
Temporal	6 h	3 h	3 h	3 h	3 h

Table 2. Scavenging coefficients used in NAME

	Rain		Snow/Ice	
	Large-Scale	Convective	Large-Scale	Convective
Orographic enhancement (seeder-feeder)	A = 3.36×10^{-4} B = 0.79	A = 3.36×10^{-4} B = 0.79	A = 1.0×10^{-3} B = 0.79	A = 1.0×10^{-3} B = 0.79
Below-cloud (washout)	A = 8.4×10^{-5} B = 0.79	A = 8.4×10^{-5} B = 0.79	A = 8.0×10^{-5} B = 0.305	A = 8.0×10^{-5} B = 0.305
In-cloud (rainout)	A = 8.4×10^{-5} B = 0.79	A = 3.36×10^{-4} B = 0.79	A = 8.0×10^{-5} B = 0.305	A = 3.36×10^{-4} B = 0.79

Table 3. ATDM and meteorology combinations available (C) and also using RAP (R).

ATDM-Meteorology	CMC	NOAA	ECMWF	UKMET	JMA
CMC-MLDPO	C				C
JMA-RATM					C,R
NOAA-HYSPLIT		C,R	C,R		C,R
UKMET-NAME			C	C	C,R
ZAMG-FLEXPART		C,R	C,R		

Table 4. Different physical removal processes accounted in MLDP0 simulations.

Type	Species Name	v_d [cm/s]	S_w [s^{-1}]	Dry Deposition	Wet Scavenging	Radioactive Decay	Gravitational Settling	Surrogate for
Gas	Ngas	0	0	No	No	No	No	Noble gases (Kr, Xe, Rn)
Particle, light	Lpar	0.1	3×10^{-5}	Yes	Yes	No	No	^{137}Cs , ^{131}I
Gas, depositing	Dgas	1	3×10^{-4}	Yes	Yes	No	No	^{131}I

Table 5. The Cs-137 deposition evaluation results using the UNSCEAR source term. Model-meteorology combinations shown in bold are used to compute the ensemble mean.

Centre	Meteorology	R	NMSE	FB	%FA2	KSP	RANK
CMC	GEM	0.71	4.27	0.05	37.8	44	3.04
CMC	MESO	0.75	5.99	-0.14	51.4	17	3.32
JMA	MESO	0.47	6.77	0.25	33.0	17	2.93
JMA	MESO-R	0.75	6.93	0.80	26.5	27	2.89
JMA (REV)	MESO	0.66	3.97	0.26	14.3	19	3.11
JMA (REV)	MESO-R	0.79	5.97	0.83	22.1	27	2.94
NOAA	ECMWF	0.85	2.43	0.02	56.4	19	3.52
NOAA	ECMWF-R	0.58	9.51	-0.46	27.8	20	2.91
NOAA	GDAS	0.88	1.58	0.23	38.3	34	3.33
NOAA	GDAS-R	0.69	6.87	-0.33	38.3	11	3.19
NOAA	MESO	0.45	9.87	0.67	46.0	15	2.72
NOAA	MESO-R	0.42	9.87	0.71	39.4	16	2.66
UKMET	UKMO	0.58	6.10	0.48	31.3	46	2.63
UKMET	ECMWF	0.83	2.16	0.42	34.4	39	3.08
UKMET	MESO	0.77	2.77	0.32	40.2	24	3.19
UKMET	MESO-R	0.67	3.73	0.28	40.7	22	3.09
ZAMG	GDAS	0.69	8.53	-0.28	49.8	27	3.06
ZAMG	GDAS-R	0.67	12.84	-0.58	34.6	9	3.06
ZAMG	ECMWF	0.75	3.26	0.22	44.4	38	3.08
ZAMG	ECMWF-R	0.78	3.77	0.41	48.6	24	3.16
ENS	ALL	0.83	2.30	0.25	43.7	37	3.19
ENS	Select	0.86	1.92	0.26	39.8	40	3.21

Table 6. The Cs-137 air concentration evaluation at the JAEA sampling site using the UNSCEAR source with the ATDM-meteorology combinations used in the ensemble shown in bold.

Centre	Meteorology	R	NMSE	FB	%FA2	KSP	RANK
CMC	GEM	0.08	67.4	-1.34	75.0	54	1.55
CMC	MESO	0.19	15.31	-0.01	82.5	34	2.52
JMA	MESO	0.46	27.49	-0.86	80.0	44	2.14
JMA	MESO-R	0.49	153.28	-1.69	57.5	66	1.30
JMA (REV)	MESO	0.21	17.34	0.02	14.29	43	2.38
JMA (REV)	MESO-R	0.06	148.84	-1.66	14.30	65	1.15
NOAA	ECMWF	0.13	41.66	-0.96	62.5	61	1.55
NOAA	ECMWF-R	0.13	42.08	-0.97	62.5	58	1.58
NOAA	GDAS	0.22	46.00	-0.89	60.0	71	1.50
NOAA	GDAS-R	0.22	46.07	-0.89	60.0	68	1.52
NOAA	MESO	0.10	126.63	-1.62	62.5	68	1.14
NOAA	MESO-R	0.10	125.62	-1.62	60.0	69	1.11
UKMET	UKMO	0.10	77.23	-1.41	70.0	54	1.46
UKMET	ECMWF	0.10	30.36	-0.74	70.0	54	1.80
UKMET	MESO	0.20	20.93	-0.42	80.0	51	2.12
UKMET	MESO-R	0.20	21.49	-0.44	80.0	51	2.11
ZAMG	GDAS	0.12	43.04	0.38	57.5	56	1.84
ZAMG	GDAS-R	0.15	43.86	0.35	57.5	56	1.86
ZAMG	ECMWF	0.06	25.66	-0.27	55.0	61	1.81
ZAMG	ECMWF-R	0.05	27.35	-0.30	42.5	71	1.57
ENS	ALL	0.11	27.37	-0.60	82.5	35	2.19
ENS	Select	0.13	24.88	-0.55	82.5	35	2.22

Table 7. Models that are part of the minimum sets retrieved based upon four statistical measures. The ranking is indicated within the brackets.

Max PCC	Min bias	min MSE	Max M1
NOAA-GDAS(1)	CMC-GEM(2)	NOAA-GDAS (1)	NOAA-ECMWF(1)
UKMET-MESO(5)	CMC-MESO(3)	UKMET-MESO (4)	UKMET-MESO(5)
UKMET-ECMWF(4)	JMA-MESO(6)	UKMET-ECMWF(3)	ZAMG-GDAS-RAP(10)
NOAA-ECMWF(2)	NOAA-GDAS-RAP(10)	NOAA-ECMWF(2)	[CMC-MESO(3)
ZAMG-ECMWF(6)	UKMET-MESO-RAP(8)	ZAMG-ECMWF(5)	NOAA-GDAS-RAP(4)
CMC-MESO(7)	ZAMG-GDAS(7)	{CMC-MESO (9) in place of UKMET-MESO in a quintuplet combination	ZAMG-ECMWF-RAP(6)]

Table 8. The (PCC) pearson correlation coefficient; (Fbias) Fractional Bias; (RMSE) Root Mean Square Error; (M1) metric M1; (Stdev Ratio) ratio of the modelled to the observed standard deviation.

	PCC	FBias	RMSE	M1	Stdev ratio
Max PCC	0.91	0.19	272.2	3.31	0.69
Min Bias	0.77	$1 \cdot 10^{-5}$	403.2	3.29	0.46
Min MSE	0.91	0.29	246.3	3.28	0.83
Max M1	0.87	0.002	344.8	3.55	0.52
Full ensemble	0.83	0.25	329.7	3.19	0.70

Table 9: Sets alternative to the minimum set.

Minimum Set	10 Member	Alternative Set	Alternative Set #2
NOAA-GDAS	NOAA-GDAS	NOAA-GDAS	NOAA-ECMWF
UKMET-MESO	NOAA-ECMWF	UKMET ECMWF	NOAA_GDAS
UKMET-ECMWF	UKMET-MESO	ZAMG-GDAS	UKMET-MESO
NOAA-ECMWF	UKMET-ECMWF	JMA-MESO-RAP	UKMET-ECMWF
ZAMG-ECMWF	ZAMG-GDAS	CMC-MESO	CMC-MESO
	ZAMG-ECMWF-RAP		JMA-MESO-RAP
	JMA-MESO		ZAMG-ECMWF-RAP
	JMA-MESO-RAP		
	CMC-GEM		
	CMC-MESO		

FIGURES

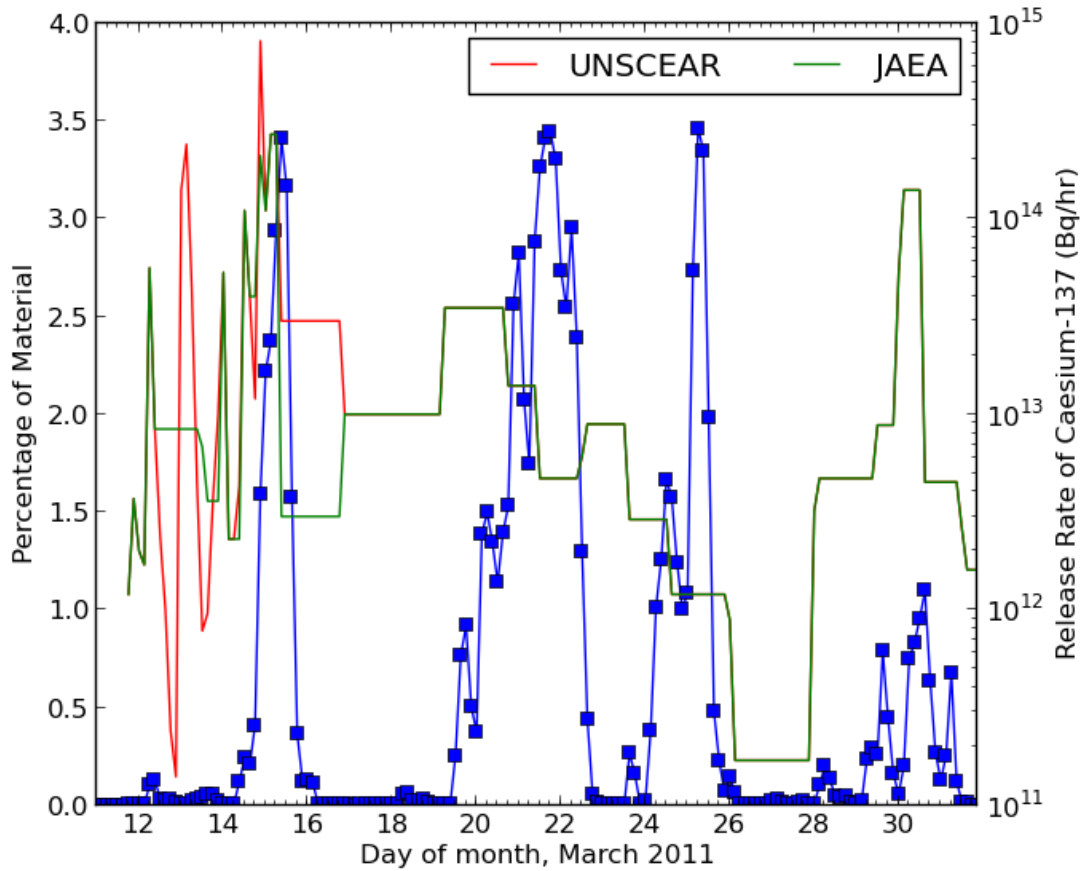
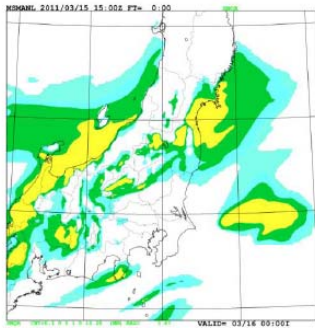


Figure 1. Time evolution of the percentage of modeled UKMET – ECMWF (blue line) total deposition (throughout March) in the region where measurements are available by each three hour source assuming that the release rate of all sources was 1Bq/hr compared to emission rates of Cs-137 for the UNSCEAR and JAEA source terms.

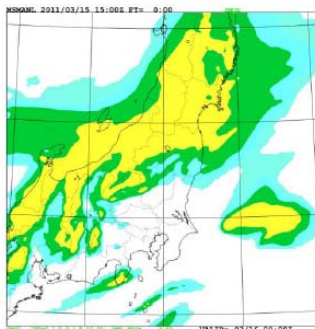
Comparison of the Accumulated Precipitation (mm)
for 1200-1500 UTC, 15 March 2011

a) Meso Analysis

1 hr average of 1200-1500 UTC

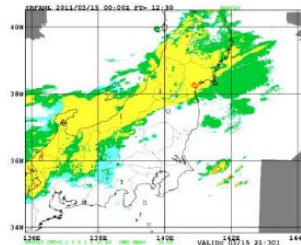


Surface precipitation (rain only)

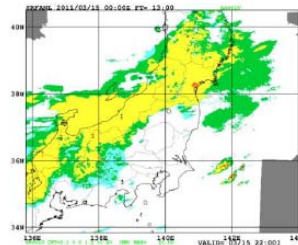


Surface precipitation (total)

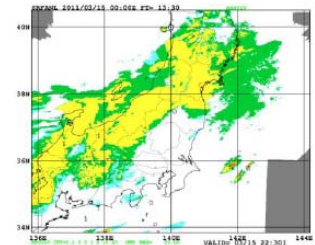
b) Radar/Rain gauge-Analyzed Precipitation



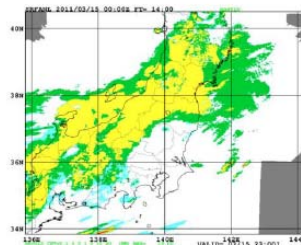
1130-1230 UTC



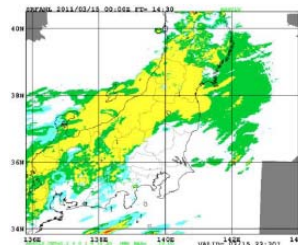
1200-1300 UTC



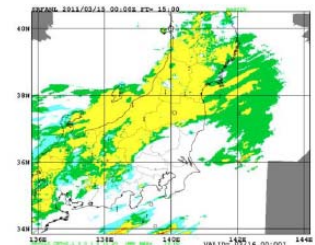
1230-1330 UTC



1300-1400 UTC



1330-1430 UTC



1400-1500 UTC

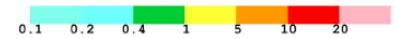


Figure 2. An example of the accumulated precipitation (mm) fields from (a) the JMA-MESO model analyses and (b) the measured precipitation estimated from radar and rain gauge observations (RAP).

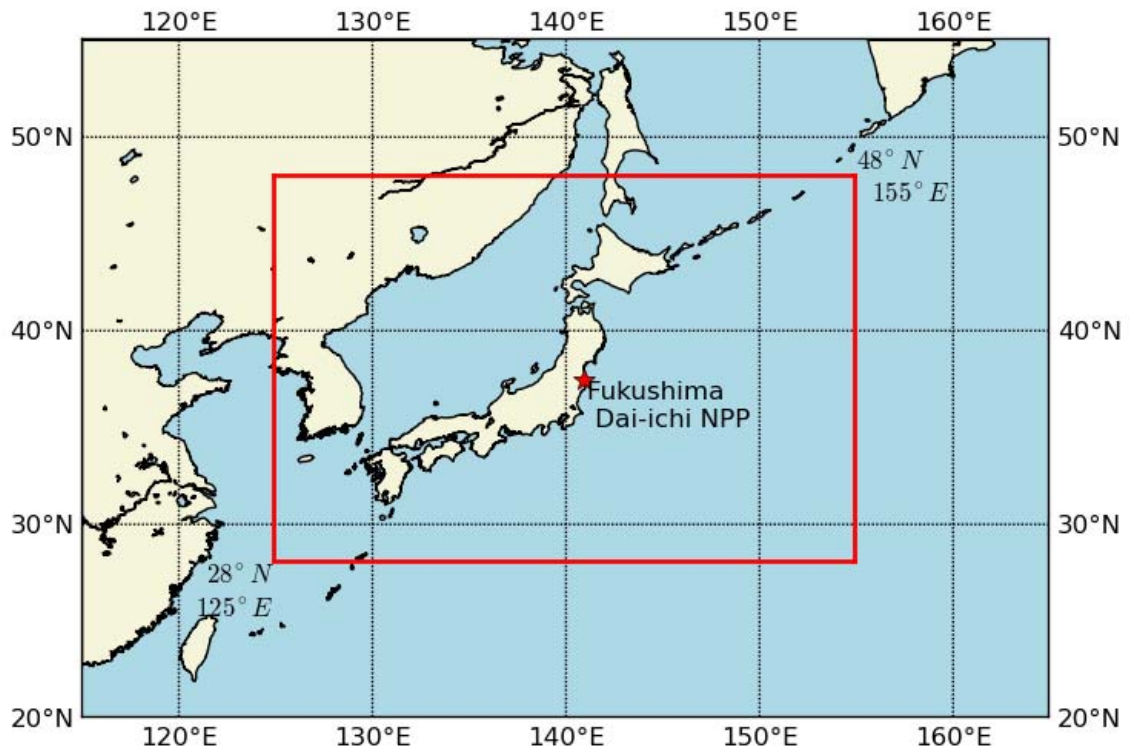


Figure 3. Regional domain (red box) over which task team calculations were performed.

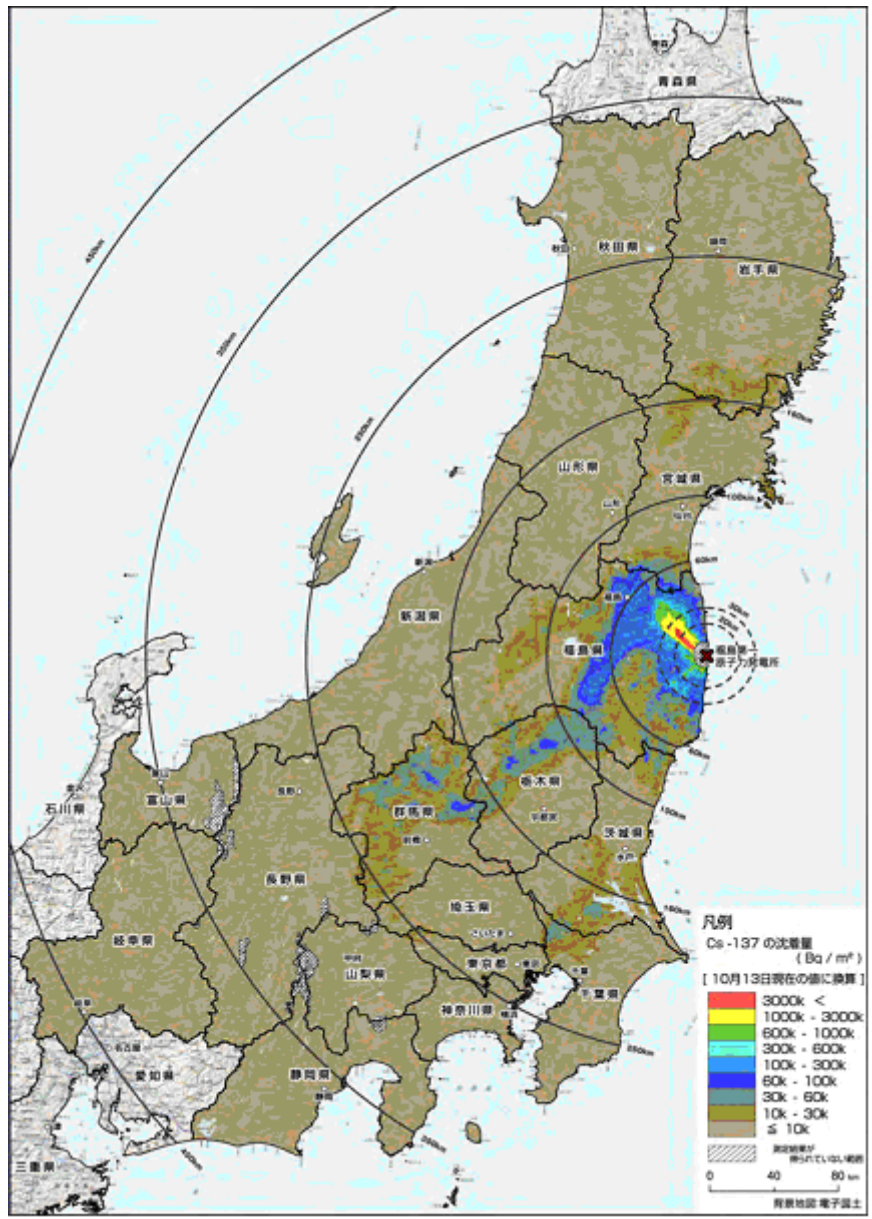


Figure 4. Regional deposition map of Cs-137 from MEXT (2011).

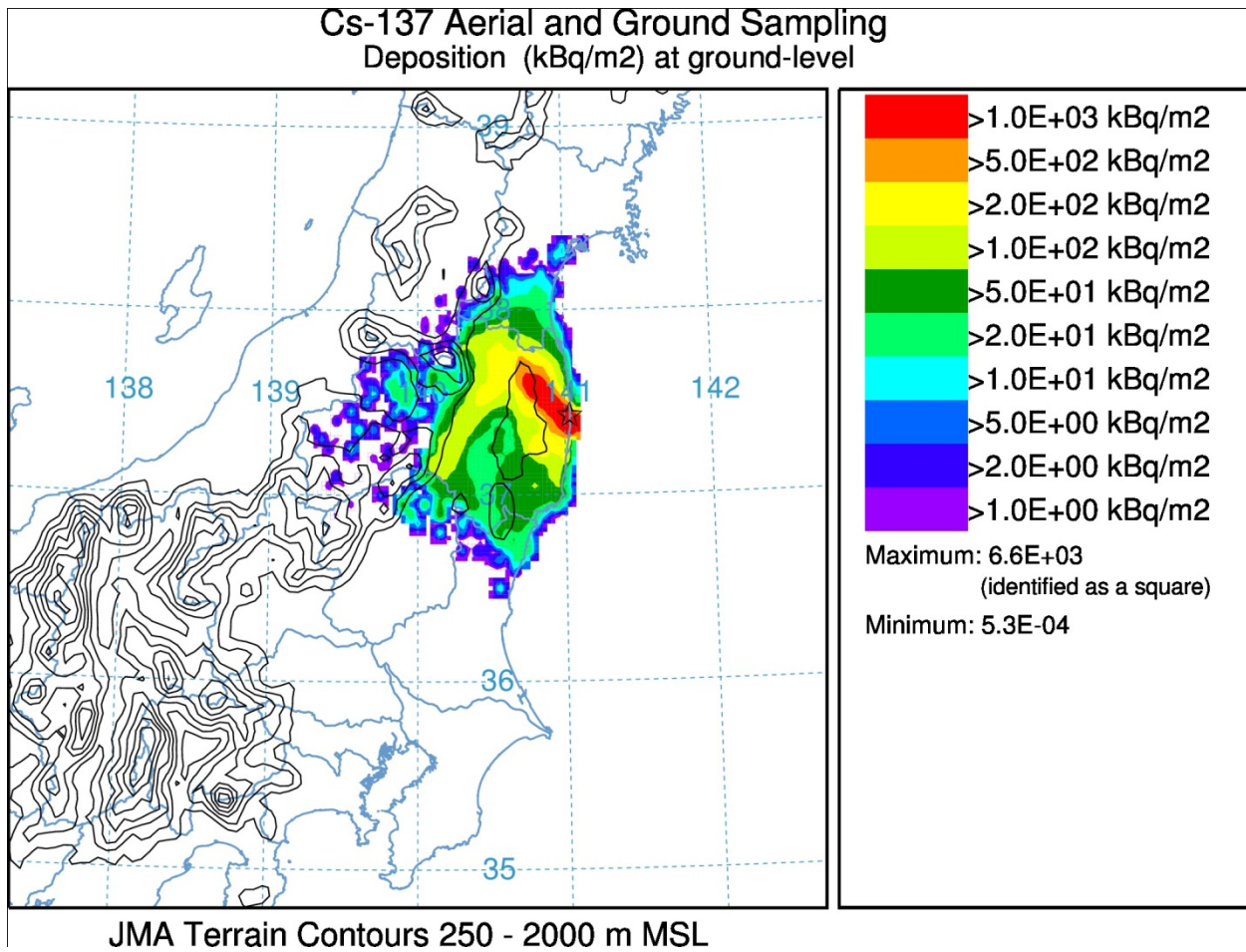


Figure 5. Measured Cs-137 deposition from ground (MEXT) and aerial (USDOE) sampling interpolated to the ATDM computational grid. Contours show the terrain elevation at 250 m intervals.

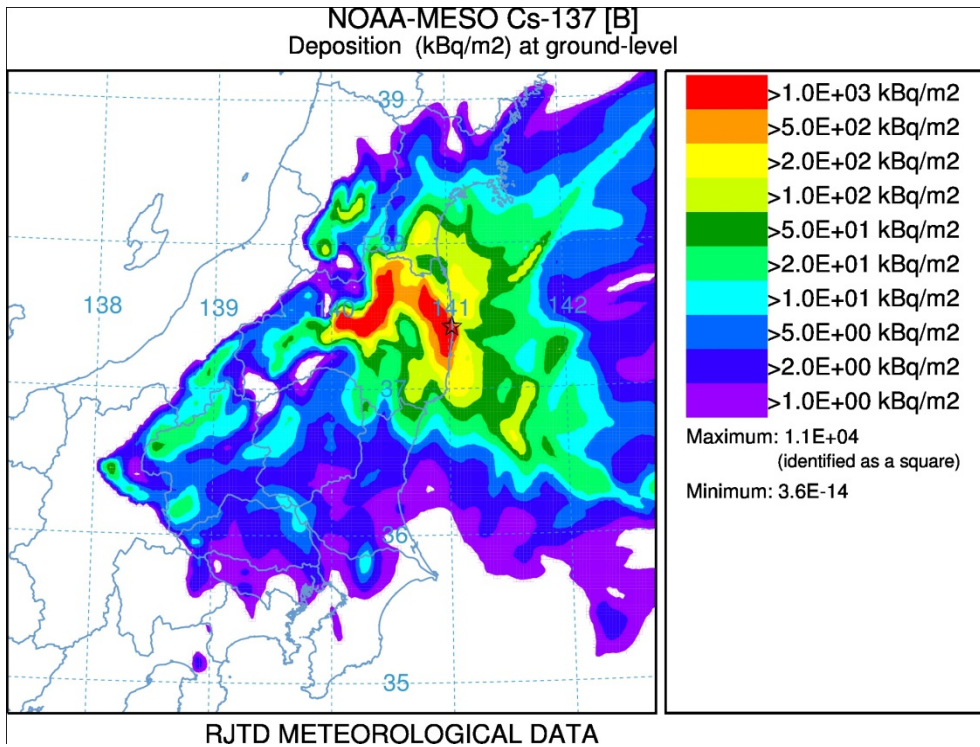
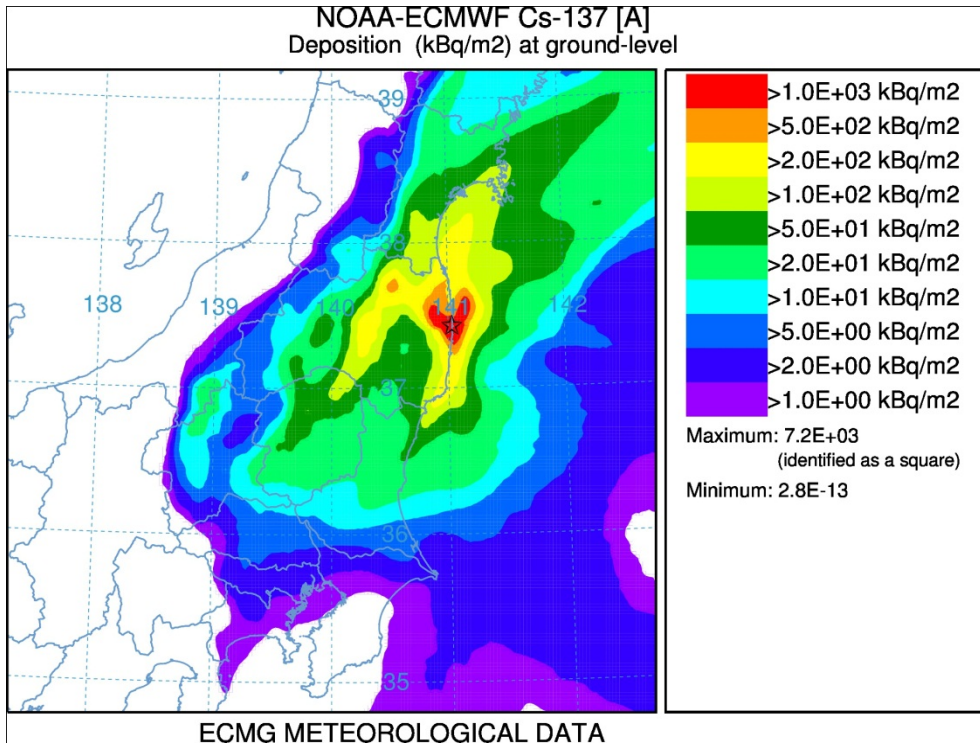


Figure 6. Calculated Cs-137 deposition using NOAA-HYSPLIT ATDM with ECMWF data (A - top) and with the JMA-MESO analysis (B - bottom).

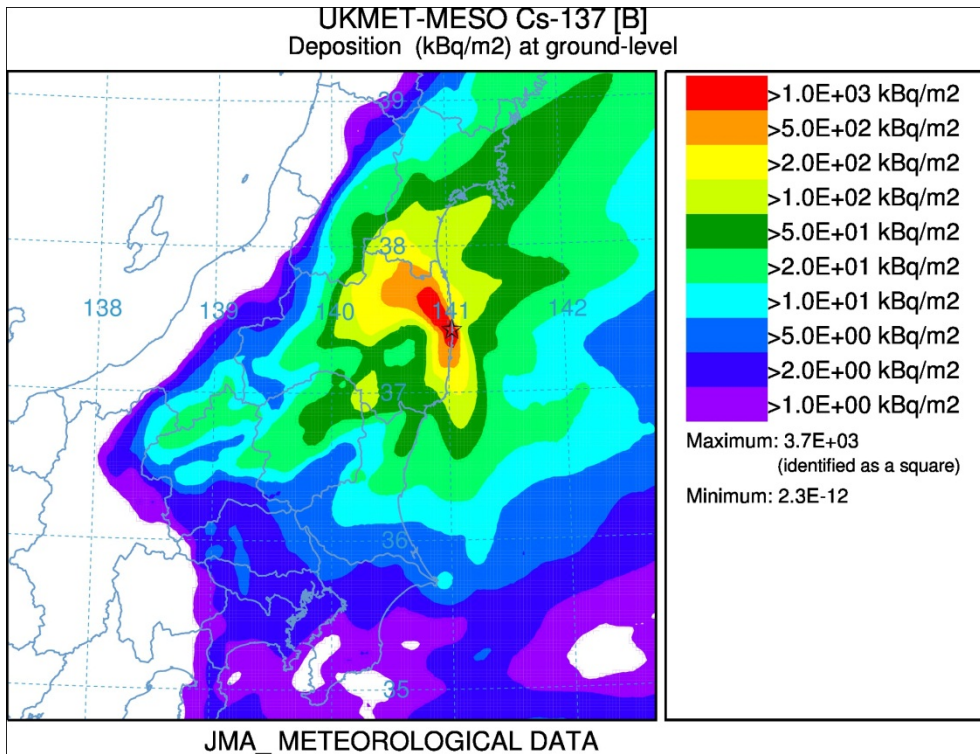
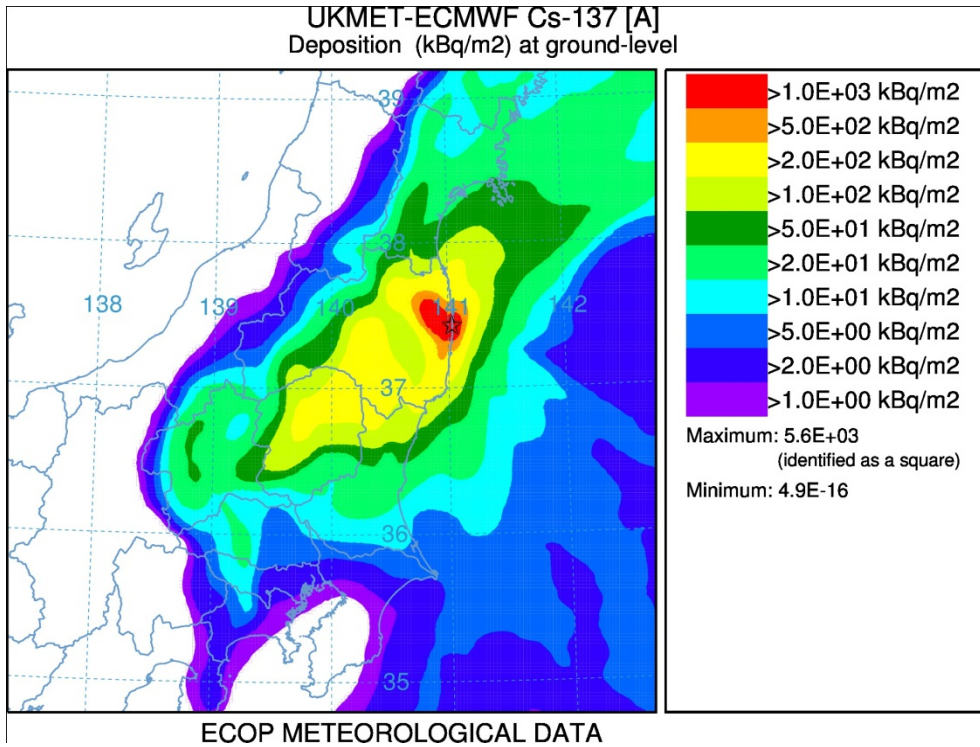


Figure 7. Calculated Cs-137 deposition using UKMET-NAME ATDM with ECMWF data (A - top) and with the JMA-MESO analysis (B - bottom).

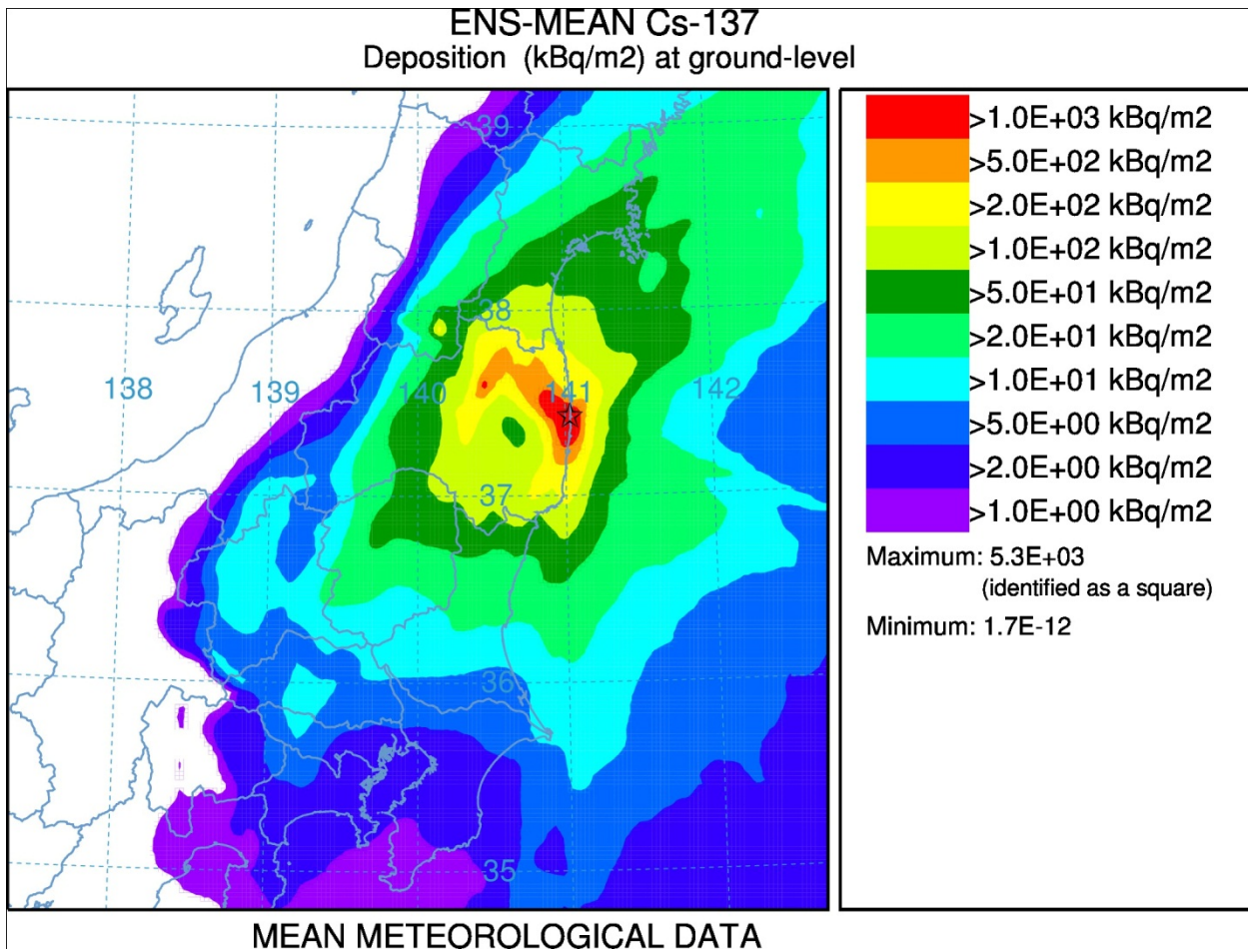


Figure 8. Calculated Cs-137 deposition using the mean of selected ten ATDM-meteorology combinations.

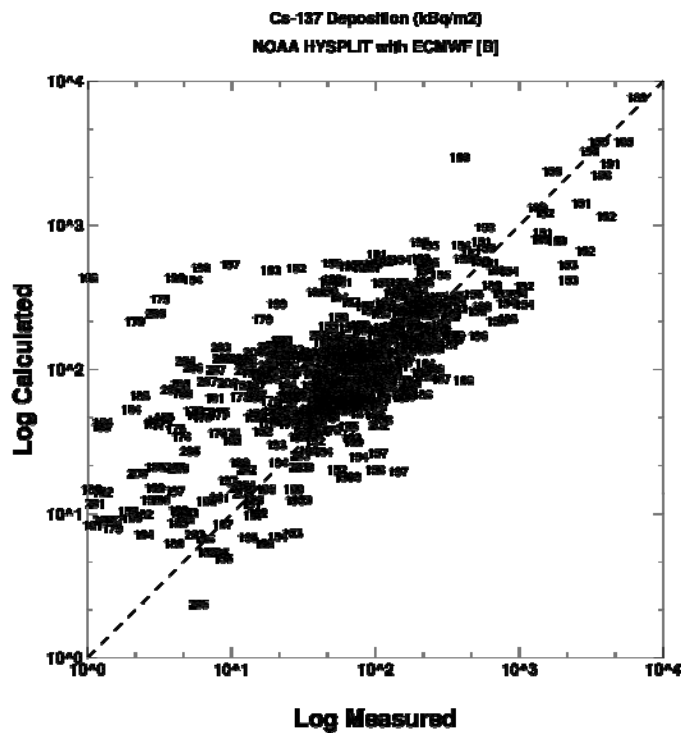
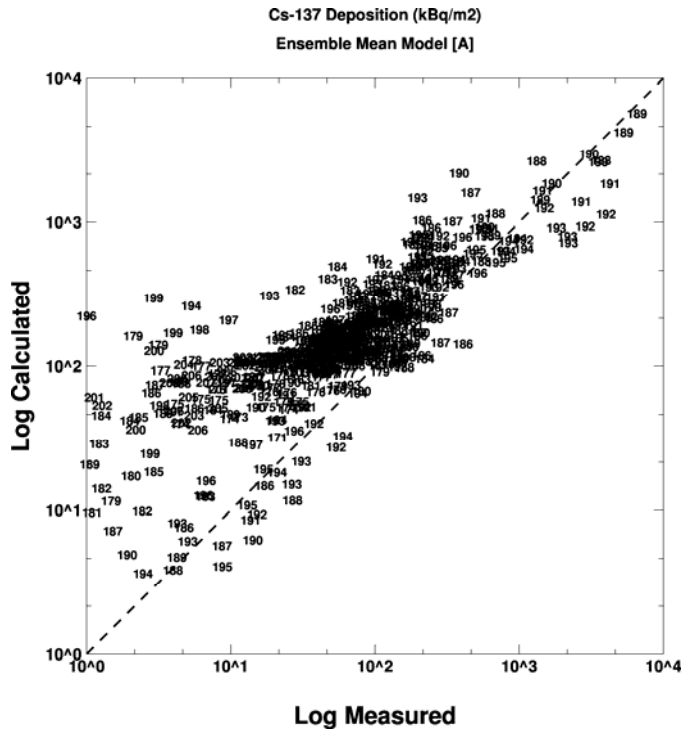


Figure 9. Scatter diagram for Cs-137 deposition for the ensemble mean model (A - top) and the NOAA-HYSPLIT using the ECMWF data, the model with the highest rank (B – bottom). Numbers represent the grid cell position in sequential units.

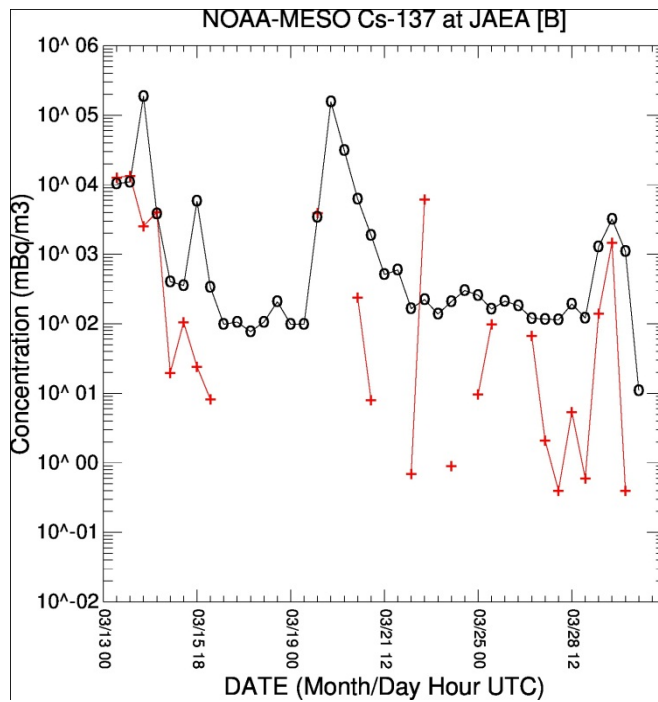
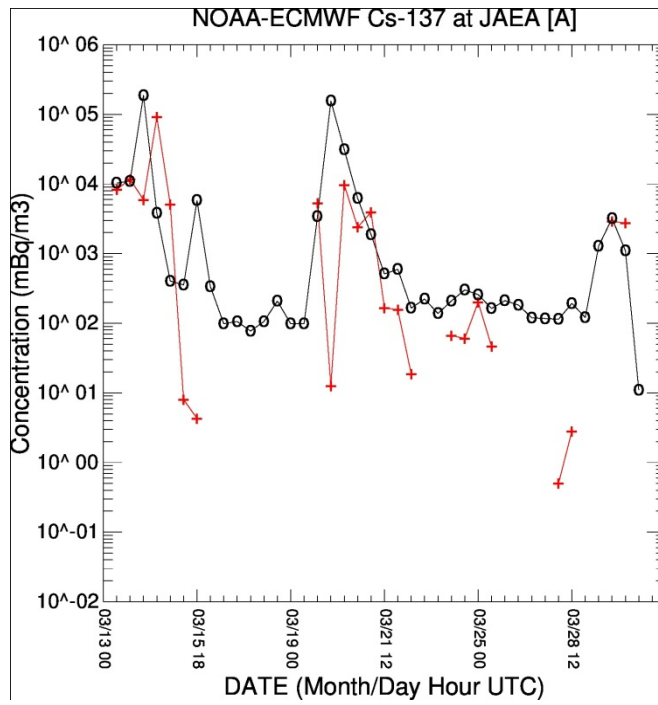


Figure 10. Calculated Cs-137 air concentrations (red +) at JAEA using NOAA-HYSPLIT ATDM with ECMWF data (A - top), with the JMA-MESO analysis (B - bottom), and the measured data at JAEA (black o).

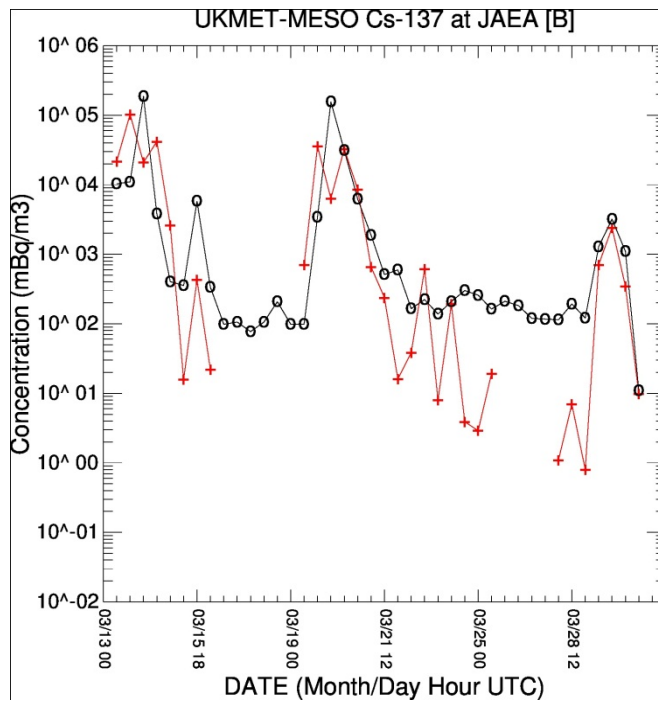
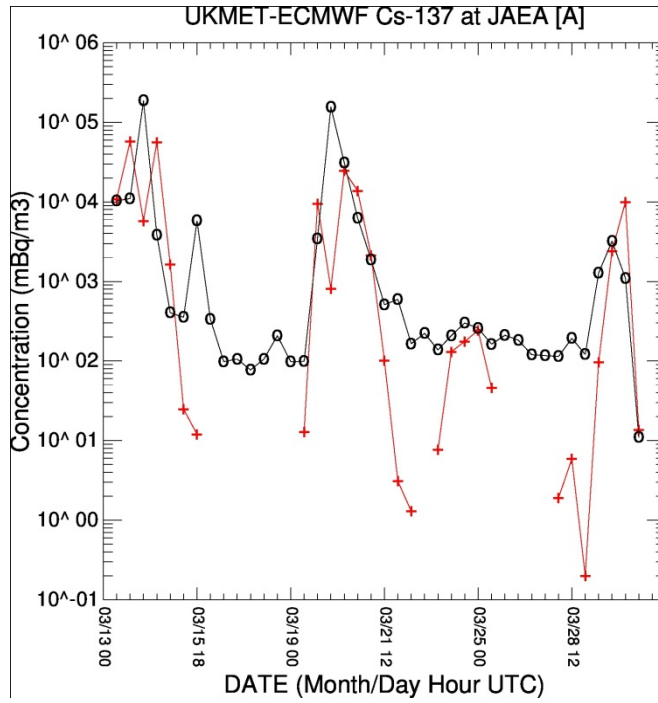


Figure 11. Calculated Cs-137 air concentrations (red +) using UKMET-NAME ATDM with ECMWF data (A - top), JMA-MESO analysis (B - bottom), and the measured data at JAEA (black o).

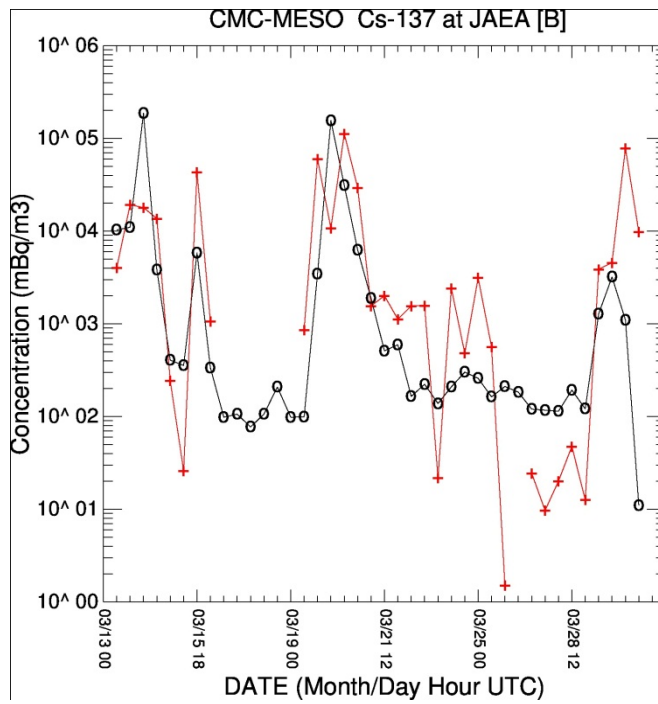
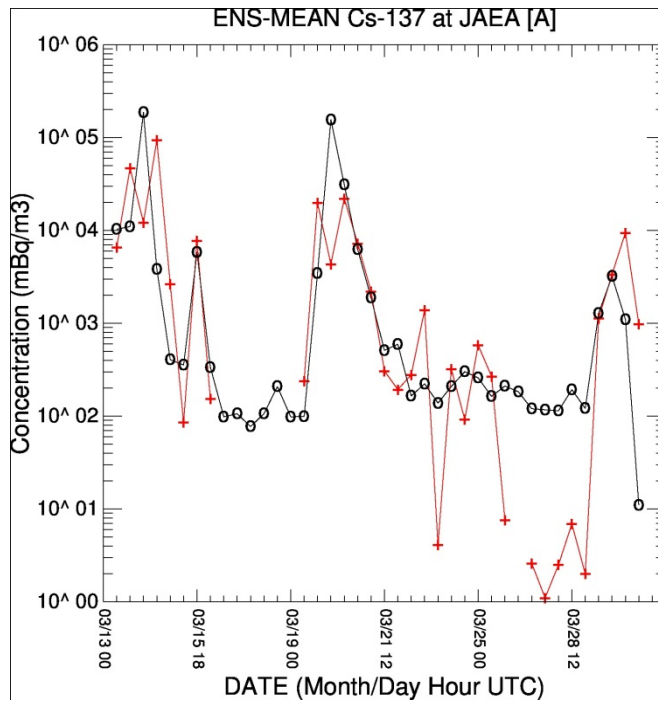


Figure 12. Calculated Cs-137 air concentrations (red +) using the ENS-Mean ATDM (A - top), CMC-MLDP0 using JMA-MESO (B - bottom), and measured data at JAEA (black o).

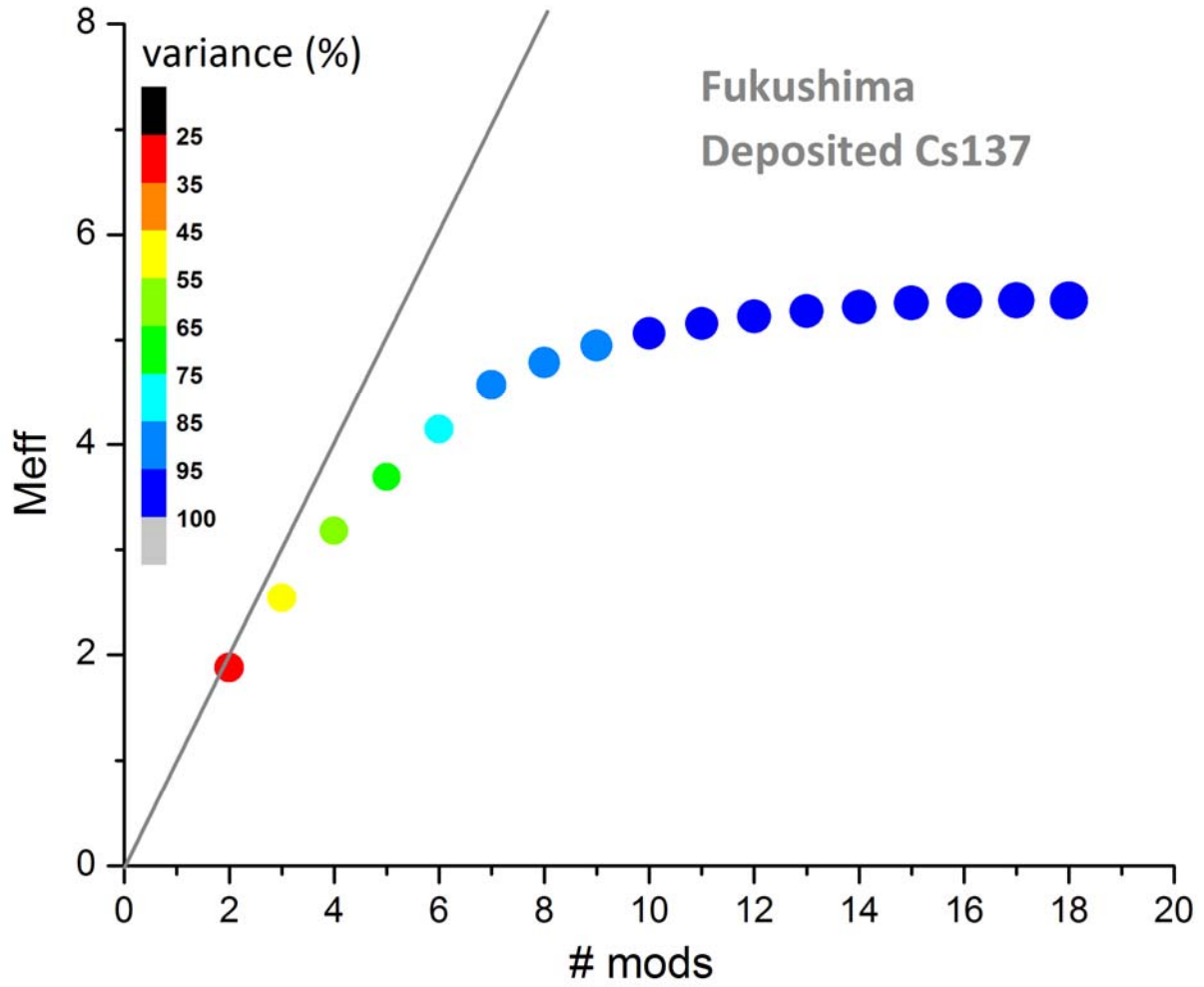


Figure 13: Variation of the effective number of members as a function of the ensemble size. The colours represent the variance of the ensemble.

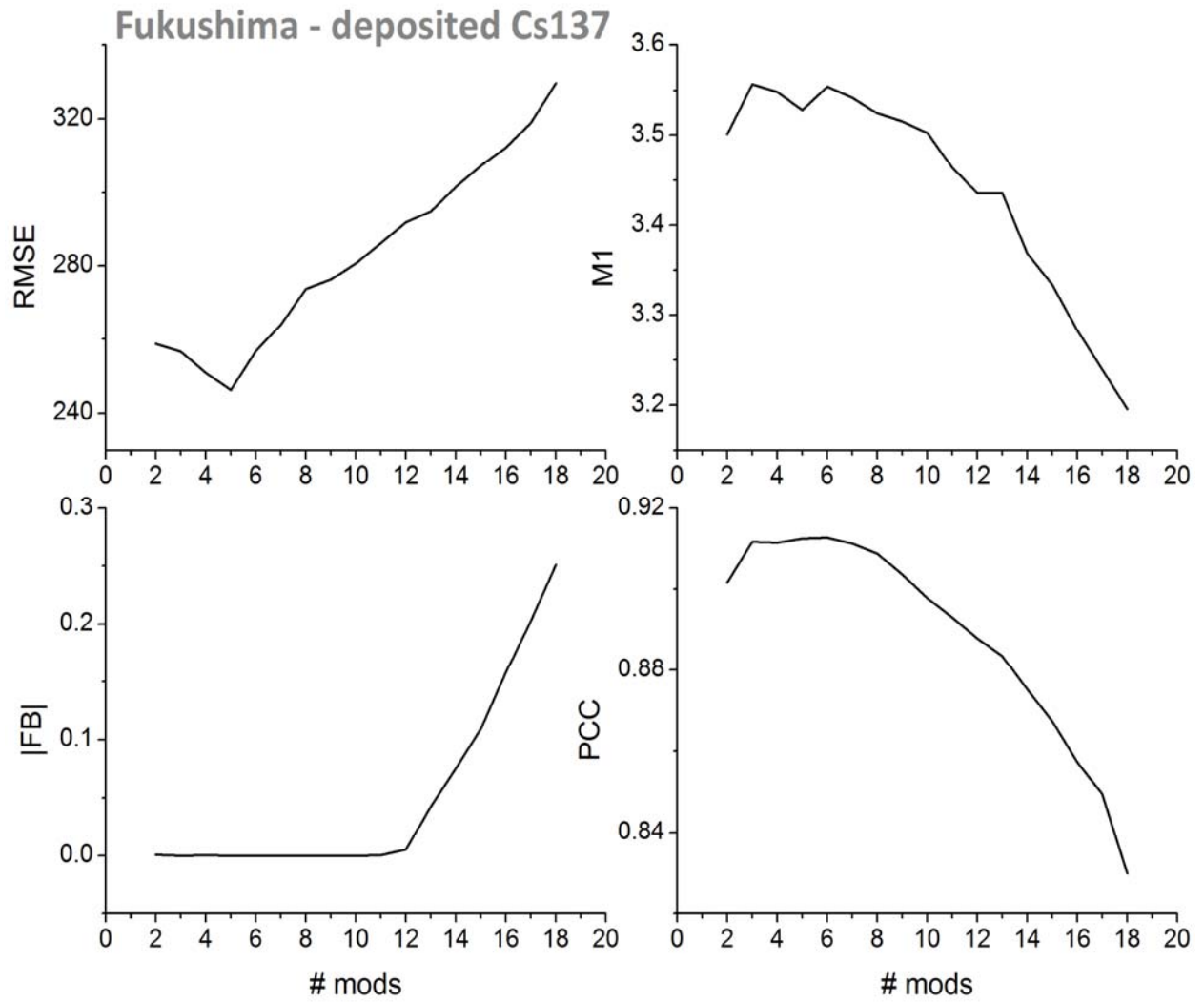


Figure 14. Clockwise from top left curves of minimum RMSE, maximum M1, maximum PCC, minimum FB, as a function of the number of models.

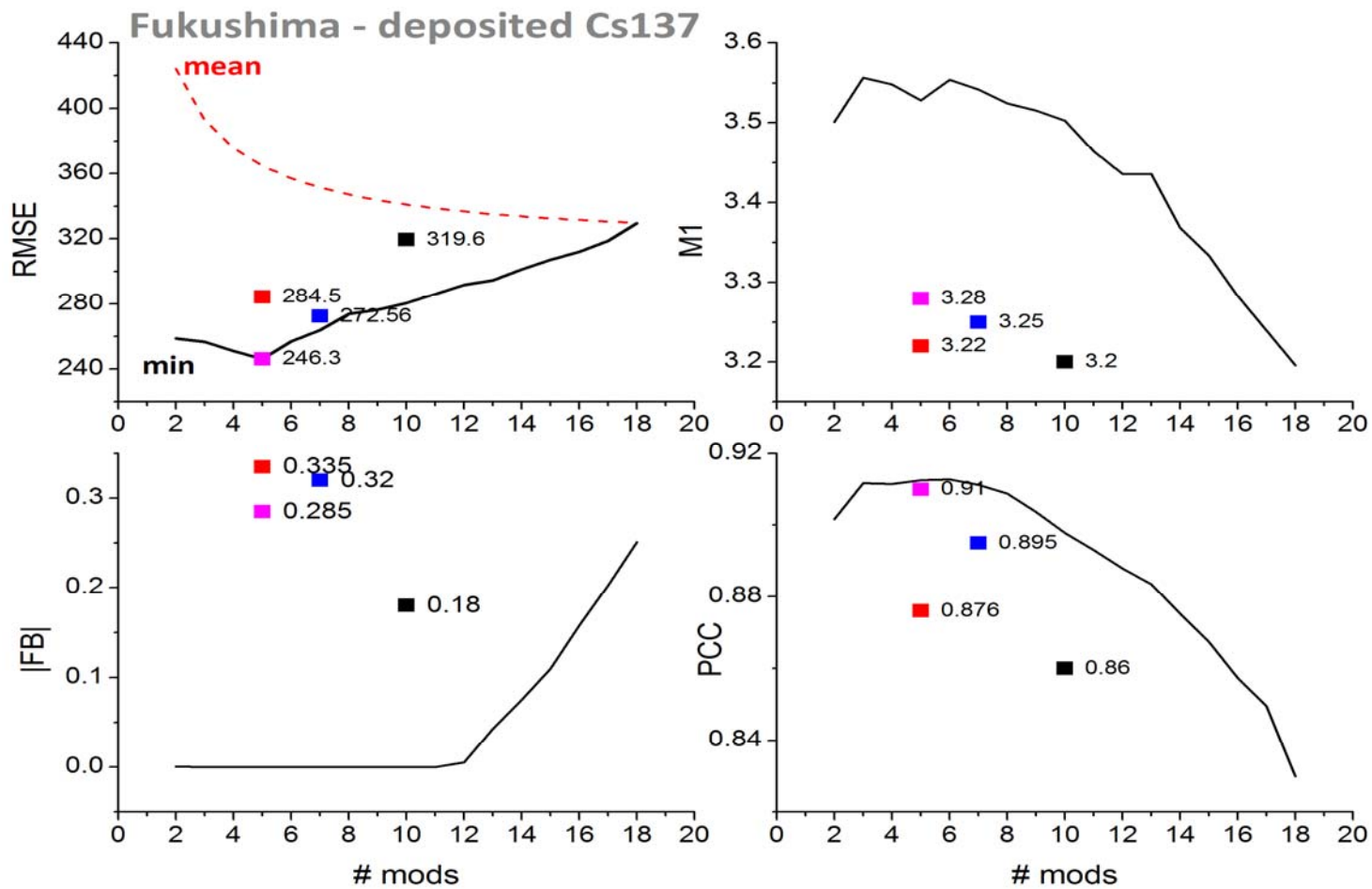


Figure 16. Performance of alternative sets (see the text for a description of the colours) compared with the minimum set and the minimum performance per number of members.

Deposition Probability Distribution

Percentiles: 5, 10, 25, 50, 75, 90, 95, and Mean

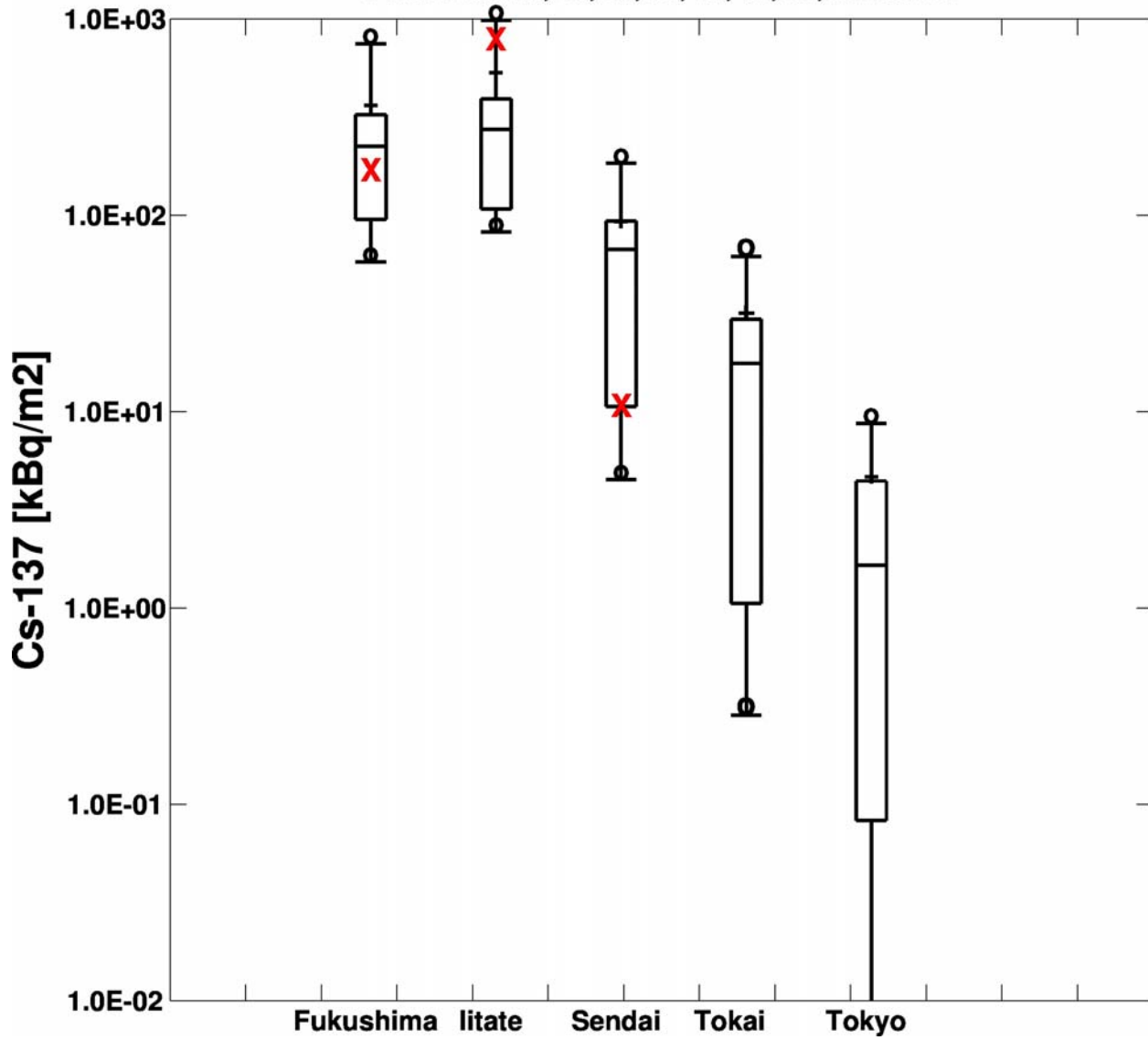


Figure 17. Box and whisker plot of the selected ensemble members for the total Cs-137 deposition at several locations. The red X shows the measured value at the grid cell corresponding to that location.

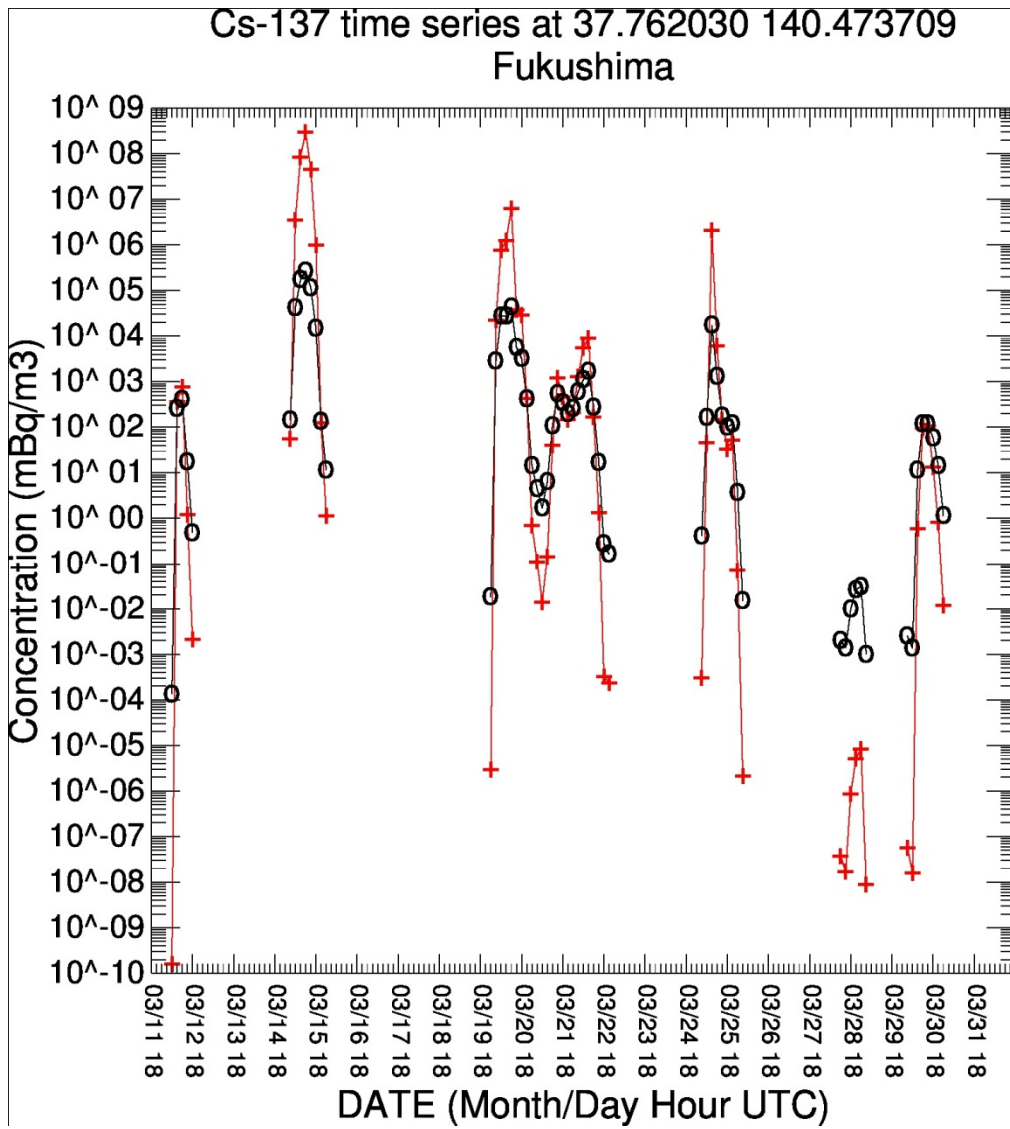


Figure 18. The calculated Cs-137 air concentration time series at Fukushima City (black o) and the ensemble variance for each calculation (red +). Variance units are concentration squared.

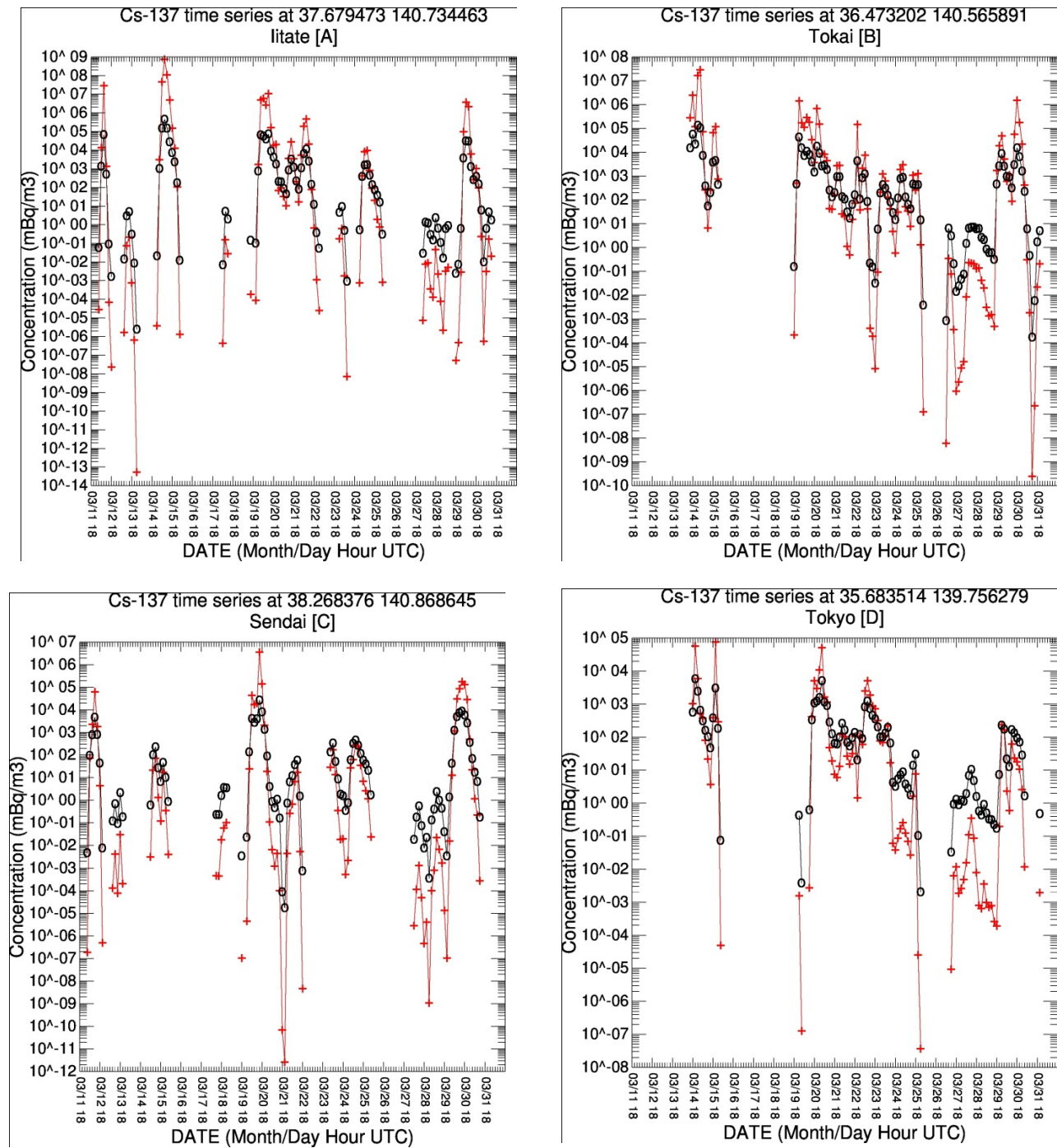


Figure 19. The calculated Cs-137 air concentration time series at litate, Sendai, Tokai, and Tokyo (black o) and the ensemble variance for each calculation (red +). Variance units are concentration squared.

Appendix A

Statistical Analysis using JAEA Source Term (Chino et al. 2011)

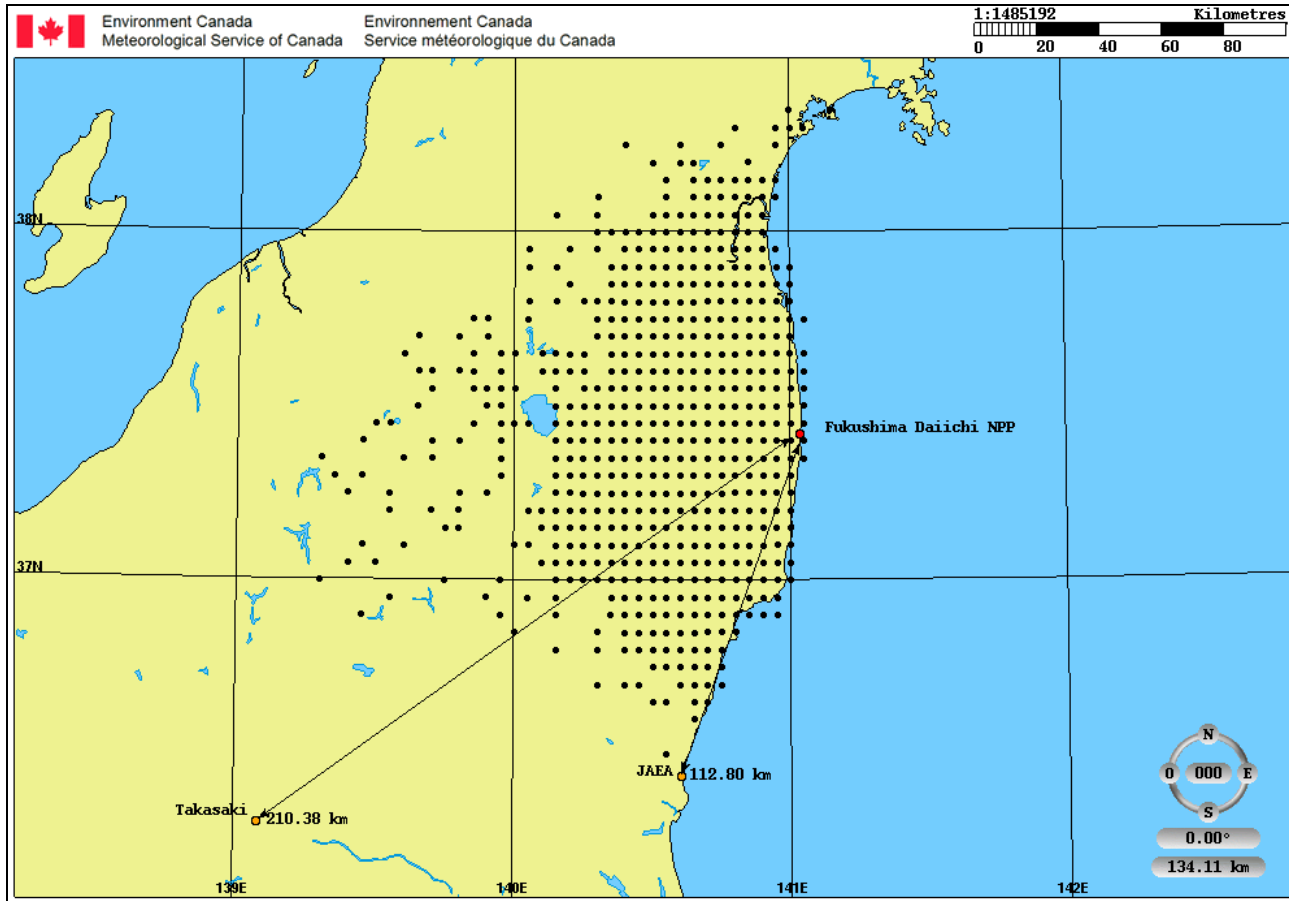
<ul style="list-style-type: none"> • Cs-137 Deposition: p. 3 • Cs-137 Air Concentrations at JAEA: p. 4 • I-131p Air Concentrations at JAEA: p. 5 • Summary and discussion: p. 6 	<ul style="list-style-type: none"> • Number of deposition measurement values: 543 • Number of air concentration measurement values at JAEA: 41
---	--

Few Definitions

<p><i>R</i>: Correlation Coefficient ($-1 \leq R \leq 1$) <i>FB</i>: Fractional Bias ($-2 \leq FB \leq +2$) <i>FMS</i>: Figure of Merit in Space (%) <i>FOEX</i>: Factor of Exceedance ($-50\% \leq FB \leq +50\%$) <i>FA2</i>: Percent C/M ± 2 (%) <i>KSP</i>: Kolmogorov-Smirnov Parameter (%)</p>	$METRIC\ 1 = R^2 + \left(1 - \left \frac{FB}{2}\right \right) + \left(\frac{FMS}{100}\right) + \left(1 - \frac{KSP}{100}\right), \quad 0 \leq METRIC\ 1 \leq 4$ $METRIC\ 2 = R^2 + \left(1 - \left \frac{FB}{2}\right \right) + \left(\frac{FA2}{100}\right) + \left(1 - \frac{KSP}{100}\right), \quad 0 \leq METRIC\ 2 \leq 4$ $METRIC\ 3 = R^2 + \left(1 - \left \frac{FB}{2}\right \right) + \left(\frac{FMS}{100}\right) + \left(1 - \left \frac{FOEX}{50}\right \right) + \left(1 - \frac{KSP}{100}\right), \quad 0 \leq METRIC\ 3 \leq 5$ $METRIC\ 4 = R^2 + \left(1 - \left \frac{FB}{2}\right \right) + \left(\frac{FMS}{100}\right) + \left(\frac{FA2}{100}\right) + \left(1 - \left \frac{FOEX}{50}\right \right) + \left(1 - \frac{KSP}{100}\right), \quad 0 \leq METRIC\ 4 \leq 6$
---	--

Deposition measurement values are represented by small black dots. Each black dot represents an averaged blend value based on ground MEXT measurements and aerial USDOE measurements on the computational modeling grid.

2 sampling sites (orange dots) for the air concentration measurement values were available: Takasaki and JAEA. Only JAEA data were used due to unresolved contamination issues at the Takasaki site.



Cs-137 Deposition – JAEA Source Term

METRIC 1	R, FB, FMS, KSP	SCORE ON 4
METRIC 2	R, FB, %FA2, KSP	SCORE ON 4
METRIC 3	R, FB, FMS, FOEX, KSP	SCORE ON 5
METRIC 4	R, FB, FMS, FOEX, %FA2, KSP	SCORE ON 6

Member No	ORGANIZATION	ATDM	NWP	R	FB	FMS	FOEX	%FA2	KSP	METRIC 1	METRIC 2	METRIC 3	METRIC 4
1	CMC	MLDP0	GEM	0.76	-0.32	100.00	11.69	48.99	19.00	3.22	2.72	3.99	4.48
2	CMC	MLDP0	MESO	0.76	-0.44	100.00	-4.33	45.12	6.00	3.30	2.75	4.21	4.66
3	JMA	RATM	MESO	0.45	-0.02	100.00	-0.46	51.01	10.00	3.09	2.60	4.08	4.59
4	JMA	RATM	MESO-R	0.77	0.54	100.00	9.67	41.99	11.00	3.22	2.63	4.02	4.44
5	NOAA	HYSPLIT	GDAS	0.87	-0.08	100.00	8.01	48.25	6.00	3.65	3.14	4.50	4.98
6	NOAA	HYSPLIT	GDAS-R	0.68	-0.57	100.00	-16.48	31.86	23.00	2.94	2.27	3.62	3.94
7	NOAA	HYSPLIT	MESO	0.55	0.38	100.00	-8.01	41.07	15.00	2.97	2.37	3.80	4.21
8	NOAA	HYSPLIT	MESO-R	0.48	0.43	100.00	-4.14	35.54	16.00	2.85	2.21	3.77	4.13
9	NOAA	HYSPLIT	ECMWF	0.83	-0.30	100.00	-12.06	46.96	10.00	3.45	2.91	4.20	4.67
10	NOAA	HYSPLIT	ECMWF-R	0.55	-0.74	100.00	-20.35	21.92	33.00	2.60	1.82	3.20	3.41
11	UKMET	NAME	UM	0.44	0.24	100.00	30.48	42.36	30.00	2.77	2.20	3.16	3.59
12	UKMET	NAME	ECMWF	0.80	0.11	100.00	19.06	54.70	25.00	3.34	2.88	3.95	4.50
13	UKMET	NAME	MESO	0.76	0.04	100.00	5.80	45.12	11.00	3.45	2.90	4.33	4.78
14	UKMET	NAME	MESO-R	0.66	0.03	100.00	6.35	34.62	9.00	3.33	2.68	4.20	4.55
15	ZAMG	FLEXPART	GDAS	0.66	-0.59	100.00	-6.17	45.12	10.00	3.05	2.49	3.92	4.37
16	ZAMG	FLEXPART	GDAS-R	0.66	-0.84	100.00	-16.85	28.36	20.00	2.82	2.10	3.48	3.76
17	ZAMG	FLEXPART	ECMWF	0.78	-0.08	100.00	9.85	59.67	15.00	3.41	3.02	4.22	4.82
18	ZAMG	FLEXPART	ECMWF-R	0.83	0.13	100.00	5.99	52.12	6.00	3.57	3.09	4.44	4.97
19	JMA (REV)	RATM	MESO	0.70	-0.04	99.63	-0.83	37.94	10.0	3.37	2.75	4.35	4.73
20	JMA (REV)	RATM	MESO-R	0.84	0.56	99.08	9.12	35.73	13.0	3.28	2.65	4.10	4.46

Cs-137 Air Concentrations at JAEA – JAEA Source Term

METRIC 1	R, FB, FMS, KSP	SCORE ON 4
METRIC 2	R, FB, %FA2, KSP	SCORE ON 4
METRIC 3	R, FB, FMS, FOEX, KSP	SCORE ON 5
METRIC 4	R, FB, FMS, FOEX, %FA2, KSP	SCORE ON 6

Member No	ORGANIZATION	ATDM	NWP	R	FB	FMS	FOEX	%FA2	KSP	METRIC 1	METRIC 2	METRIC 3	METRIC 4
1	CMC	MLDP0	GEM	0.07	-1.37	73.17	-30.95	7.14	53.00	1.52	0.86	1.90	1.97
2	CMC	MLDP0	MESO	0.23	-0.09	80.49	-4.76	16.67	34.00	2.47	1.83	3.38	3.54
3	JMA	RATM	MESO	0.51	-0.82	80.00	-21.43	21.43	43.00	2.22	1.63	2.79	3.01
4	JMA	RATM	MESO-R	0.59	-1.66	57.50	-45.24	4.76	64.00	1.46	0.93	1.55	1.60
5	NOAA	HYSPLIT	GDAS	0.10	-1.37	60.00	-42.86	7.14	69.00	1.24	0.71	1.38	1.45
6	NOAA	HYSPLIT	GDAS-R	0.10	-1.38	60.00	-42.86	7.14	67.00	1.25	0.72	1.39	1.46
7	NOAA	HYSPLIT	MESO	0.15	-1.63	62.50	-40.48	11.90	67.00	1.16	0.66	1.35	1.47
8	NOAA	HYSPLIT	MESO-R	0.15	-1.63	60.00	-40.48	9.52	67.00	1.14	0.63	1.33	1.42
9	NOAA	HYSPLIT	ECMWF	0.27	-1.33	62.50	-35.71	11.90	60.00	1.43	0.93	1.72	1.84
10	NOAA	HYSPLIT	ECMWF-R	0.27	-1.35	62.50	-35.71	16.67	60.00	1.43	0.96	1.71	1.88
11	UKMET	NAME	UM	0.06	-1.42	65.85	-30.95	19.05	53.00	1.42	0.95	1.80	1.99
12	UKMET	NAME	ECMWF	0.13	-0.93	68.29	-28.57	21.43	53.00	1.70	1.24	2.13	2.35
13	UKMET	NAME	MESO	0.24	-0.50	80.00	-28.57	16.67	52.00	2.09	1.45	2.52	2.68
14	UKMET	NAME	MESO-R	0.24	-0.53	80.00	-30.95	16.67	52.00	2.07	1.44	2.45	2.62
15	ZAMG	FLEXPART	GDAS	0.17	-0.37	57.50	-35.71	14.29	57.00	1.85	1.42	2.13	2.28
16	ZAMG	FLEXPART	GDAS-R	0.18	-0.43	57.50	-35.71	14.29	55.00	1.84	1.41	2.13	2.27
17	ZAMG	FLEXPART	ECMWF	0.12	-0.54	52.50	-35.71	11.90	60.00	1.67	1.26	1.96	2.07
18	ZAMG	FLEXPART	ECMWF-R	0.08	-0.55	42.50	-35.71	7.14	69.00	1.46	1.11	1.75	1.82
19	JMA (REV)	RATM	MESO	0.39	-0.40	77.5	-19.05	14.29	43.00	2.30	1.67	2.92	3.06
20	JMA (REV)	RATM	MESO-R	0.07	-1.68	62.5	-42.86	9.52	67.00	1.12	0.59	1.26	1.36

I-131p Air Concentrations at JAEA – JAEA Source Term

METRIC 1	R, FB, FMS, KSP	SCORE ON 4
METRIC 2	R, FB, %FA2, KSP	SCORE ON 4
METRIC 3	R, FB, FMS, FOEX, KSP	SCORE ON 5
METRIC 4	R, FB, FMS, FOEX, %FA2, KSP	SCORE ON 6

Member No	ORGANIZATION	ATDM	NWP	R	FB	FMS	FOEX	%FA2	KSP	METRIC 1	METRIC 2	METRIC 3	METRIC 4
1	CMC	MLDPO	GEM	0.10	-1.50	75.61	-38.10	9.52	50.00	1.52	0.86	1.75	1.85
2	CMC	MLDPO	MESO	0.42	-0.59	82.93	-16.67	21.43	34.00	2.37	1.76	3.04	3.25
3	JMA	RATM	MESO	0.47	-0.96	78.05	-30.95	14.29	43.00	2.09	1.45	2.47	2.62
4	JMA	RATM	MESO-R	0.67	-1.71	60.98	-45.24	0.00	60.00	1.60	0.99	1.70	1.70
5	NOAA	HYSPLIT	GDAS	0.11	-1.45	58.54	-42.86	7.14	69.00	1.19	0.67	1.33	1.40
6	NOAA	HYSPLIT	GDAS-R	0.11	-1.45	58.54	-42.86	7.14	65.00	1.22	0.71	1.37	1.44
7	NOAA	HYSPLIT	MESO	0.08	-1.54	60.98	-38.10	9.52	69.00	1.15	0.64	1.39	1.49
8	NOAA	HYSPLIT	MESO-R	0.08	-1.54	58.54	-40.48	9.52	67.00	1.15	0.66	1.34	1.44
9	NOAA	HYSPLIT	ECMWF	0.31	-1.45	63.41	-38.10	9.52	55.00	1.46	0.92	1.69	1.79
10	NOAA	HYSPLIT	ECMWF-R	0.31	-1.45	63.41	-38.10	9.52	53.00	1.47	0.94	1.71	1.81
11	UKMET	NAME	UM	0.04	-1.53	70.73	-38.10	7.14	55.00	1.40	0.76	1.63	1.70
12	UKMET	NAME	ECMWF	0.16	-1.14	73.17	-35.71	16.67	55.00	1.64	1.07	1.92	2.09
13	UKMET	NAME	MESO	0.26	-0.70	80.49	-33.33	9.52	52.00	2.00	1.29	2.34	2.43
14	UKMET	NAME	MESO-R	0.25	-0.72	80.49	-35.71	9.52	52.00	1.99	1.28	2.27	2.37
15	ZAMG	FLEXPART	GDAS	0.20	-0.46	56.10	-33.33	11.90	60.00	1.77	1.33	2.10	2.22
16	ZAMG	FLEXPART	GDAS-R	0.21	-0.53	56.10	-35.71	14.29	60.00	1.74	1.32	2.03	2.17
17	ZAMG	FLEXPART	ECMWF	0.14	-0.65	53.66	-35.71	4.76	57.00	1.66	1.17	1.95	1.99
18	ZAMG	FLEXPART	ECMWF-R	0.10	-0.65	46.34	-35.71	2.38	69.00	1.46	1.02	1.74	1.77
19	JMA (REV)	RATM	MESO	0.14	-0.54	75.61	-23.81	16.67	40.00	2.11	1.52	2.63	2.80
20	JMA (REV)	RATM	MESO-R	0.02	-1.60	60.98	-42.86	4.76	65.00	1.16	0.60	1.30	1.35

Summary and Discussion

- It is difficult to make a valid correlation between deposition scores and air concentration scores because deposition measurements are not situated at the same geographical locations as the airborne concentration measurements. It is possible that for a specific model member, the scores are good for deposition and bad for air concentrations (or vice versa) due to different meteorological conditions/patterns over the spatial-temporal domain. The number of deposition measurements (543) is much greater than the number of air concentration measurements (41 at JAEA).
- The following table shows the top 4 model members for different metrics.
- The best quadruplet model members are not the same for deposition measurement-model comparisons that for air concentration measurement-model comparisons.
- The best model members for Cs-137 deposition are the ones using GDAS, ECMWF, ECMWF-R and MESO meteorology.
- The best model members for air concentrations all use MESO meteorology except for one GDAS.
- **MESO** meteorology is in **bold** characters in the table.

Using JAEA Source Term	Metric 1	Metric 2	Metric 3	Metric 4
Cs-137 Deposition	1. NOAA-HYSPLIT-GDAS 2. ZAMG-FLEXPART-ECMWF-R 3. NOAA-HYSPLIT-ECMWF 4. UKMET-NAME- MESO	1. NOAA-HYSPLIT-GDAS 2. ZAMG-FLEXPART-ECMWF-R 3. NOAA-HYSPLIT-ECMWF 4. NOAA-HYSPLIT-ECMWF	1. NOAA-HYSPLIT-GDAS 2. ZAMG-FLEXPART-ECMWF-R 3. JMA(REV)-RATM- MESO 4. UKMET-NAME- MESO	1. NOAA-HYSPLIT-GDAS 2. ZAMG-FLEXPART-ECMWF-R 3. ZAMG-FLEXPART-ECMWF 4. UKMET-NAME- MESO
Cs-137 Air Concentrations at JAEA	1. CMC-MLDP0- MESO 2. JMA(REV)-RATM- MESO 3. JMA-RATM- MESO 4. UKMET-NAME- MESO	1. CMC-MLDP0- MESO 2. JMA(REV)-RATM- MESO 3. JMA-RATM- MESO 4. UKMET-NAME- MESO	1. CMC-MLDP0- MESO 2. JMA(REV)-RATM- MESO 3. JMA-RATM- MESO 4. UKMET-NAME- MESO	1. CMC-MLDP0- MESO 2. JMA(REV)-RATM- MESO 3. JMA-RATM- MESO 4. UKMET-NAME- MESO
I-131p Air Concentrations at JAEA	1. CMC-MLDP0- MESO 2. JMA(REV)-RATM- MESO 3. JMA-RATM- MESO 4. UKMET-NAME- MESO	1. CMC-MLDP0- MESO 2. JMA(REV)-RATM- MESO 3. JMA-RATM- MESO 4. ZAMG-FLEXPART-GDAS	1. CMC-MLDP0- MESO 2. JMA(REV)-RATM- MESO 3. JMA-RATM- MESO 4. UKMET-NAME- MESO	1. CMC-MLDP0- MESO 2. JMA(REV)-RATM- MESO 3. JMA-RATM- MESO 4. UKMET-NAME- MESO